RIS-aided Near-Field Localization under Phase-Dependent Amplitude Variations

Cuneyd Ozturk, *Student Member, IEEE*, Musa Furkan Keskin, *Member, IEEE*, Henk Wymeersch, *Senior Member, IEEE*, and Sinan Gezici, *Senior Member, IEEE*

***Abstract*—We investigate the problem of reconfigurable intelligent surface (RIS)-aided near-field localization of a user equipment (UE) served by a base station (BS) under phase-dependent amplitude variations at each RIS element. Through a misspecified Cramér-Rao bound (MCRB) analysis and a resulting lower bound (LB) on localization, we show that when the UE is unaware of amplitude variations (i.e., assumes unit-amplitude responses), severe performance penalties can arise, especially at high signal-to-noise ratios (SNRs). Leveraging Jacobi-Anger expansion to decouple range-azimuth-elevation dimensions, we develop a low-complexity approximated mismatched maximum likelihood (AMML) estimator, which is asymptotically tight to the LB. To mitigate performance loss due to model mismatch, we propose to jointly estimate the UE location and the RIS amplitude model parameters. The corresponding Cramér-Rao bound (CRB) is derived, as well as an iterative refinement algorithm, which employs the AMML method as a subroutine and alternatingly updates individual parameters of the RIS amplitude model. Simulation results indicate fast convergence and performance close to the CRB. The proposed method can successfully recover the performance loss of the AMML under a wide range of RIS parameters and effectively calibrate the RIS amplitude model online with the help of a user that has an a-priori unknown location.**

***Index Terms*—Localization, reconfigurable intelligent surfaces, hardware impairments, misspecified Cramér-Rao bound (MCRB), maximum likelihood estimator, Jacobi-Anger expansion.**

I. Introduction

Among the envisioned technological enablers for 6G, three stand out as being truly disruptive: the transition from 30 GHz to beyond 100 GHz (the so-called higher mmWave and lower THz bands) [1]–[3], the convergence of communication, localization, and sensing (referred to as integrated sensing and communication (ISAC) or integrated sensing, localization, and communication (ISLAC)) [4]–[8], and the introduction of reconfigurable intelligent surfaces (RISs) [9]–[11]. RISs are large passive metasurfaces, comprising arrays of programmable reflective unit cells, and have the ability to shape the propagation environment by judiciously adjusting the phase shifts at each reflecting element, thus locally boosting the signal-to-noise ratio (SNR) to improve communication quality [12]–[15]. This is especially relevant in beyond 100 GHz to overcome sudden drops in rate caused by temporary blockage of the line-of-sight (LoS) path [14], [16]. In order to provide enhanced performance in downlink single- and multi-user systems, passive reflect beamforming at the RIS can be optimized, potentially together with active beamforming at the base station (BS), to maximize energy efficiency [15], [17], sum-rate [18]–[20] and mutual information [21], as well as to minimize total transmit power at the BS [22], [23].

In parallel with the benefits for communications, RISs can similarly improve localization performance [24]. Stronger even, RISs with known position and orientation enjoy the ability to enable localization in scenarios where it would otherwise be impossible [25]. In this respect, the large aperture of the RIS has several interesting properties. First of all, the SNR-boosting provides accurate delay measurements when wideband signals are used [2], [26]. Secondly, the large number of elements provides high resolution in angle-of-arrival (AoA) (for uplink localization) or angle-of-departure (AoD) (for downlink localization) [2]. Third, when the user equipment (UE) is close to the RIS (in the sense that the distance to the RIS is of similar order as the physical size of the RIS), wavefront curvature effects (so-called geometric near-field) can be harnessed to localize the user [16], [24], [27]–[31], even when the LoS path between the BS and UE is blocked, irrespective of whether wideband or narrowband signals are used. Moreover, closed-form RIS phase profile designs taking into account the spherical wavefront can be employed to improve localization accuracy under near-field conditions [26], [32]. As a step further, joint benefits in ISLAC applications can be reaped via RIS phase profile adjustment by simultaneous optimization of localization and communications metrics [33].

In ISLAC scenarios, critical to the effective utilization of RIS is the control of individual RIS elements, commonly through phase shifters, which provide element-by-element control with a certain resolution and allow coherent combination of paths to/from the RIS [13], [20]. For localization, in contrast to communication, the receiver should be equipped with the knowledge of the RIS phase profiles to apply suitable high-accuracy processing methods [11]. The ability to modulate the RIS phase profiles brings additional benefits, such as separating the controlled and uncontrolled multipath through temporal coding [34]. Hence, the ability to control the RIS in a precise and known manner is essential for ISLAC applications, which necessitates the availability of accurate and simple RIS phase control models. Such models should ideally account for the per-element response [35], the finite quantization of the control [13], [36], mutual coupling [37], calibration effects, and power losses. Most studies on RIS localization have considered ideal phase shifters (e.g. [16], [25]–[28], [30], [38]), omitting the listed impairments. How these proposed localization approaches fare under these impairments is both unknown and important.

C. Ozturk is with the Department of Electrical and Computer Engineering, Northwestern University, Evanston, IL 60208, USA, E-mail: cuneyd.ozturk@northwestern.edu

M. F. Keskin and H. Wymeersch are with the Department of Electrical Engineering, Chalmers University of Technology, Sweden, E-mails: {furkan,henkw}@chalmers.se

S. Gezici is with the Department of Electrical and Electronics Engineering, Bilkent University, Ankara, 06800, Turkey, E-mail: gezici@ee.bilkent.edu.tr

This work was supported, in part, by the EU H2020 RISE-6G project under grant 101017011 and by the MSCA-IF grant 888913 (OTFS-RADCOM).

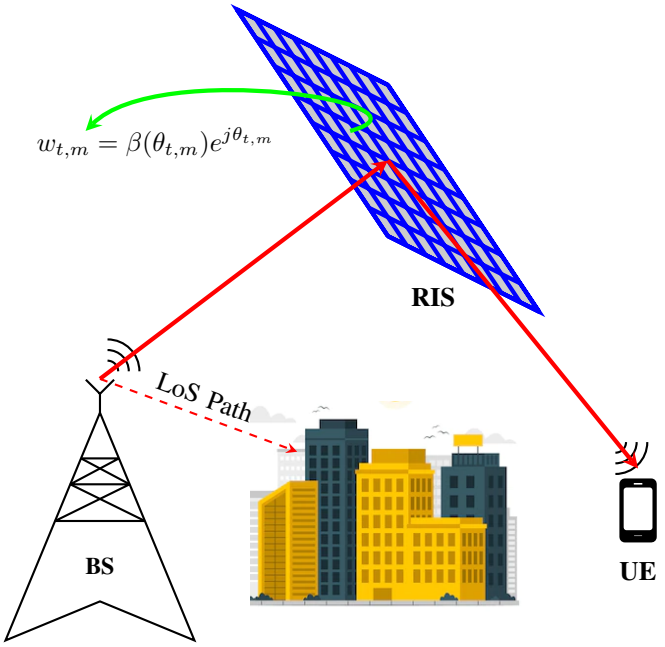

Fig. 1. Configuration of a RIS-aided localization system with LoS blockage.

In this manuscript, we investigate the problem of RIS-aided geometric near-field localization of a single-antenna UE served by a single-antenna BS under LoS blockage [16], [28], [30], [39], considering a realistic RIS amplitude model [35], which relies on equivalent circuit models of individual reflecting elements. Specifically, we quantify degradation in localization performance due to mismatch between an *ideal model* with unit-amplitude RIS element responses and a *realistic model* with phase-dependent amplitude variations [35], [40], by resorting to the misspecified Cramér-Rao bound (MCRB) analysis [41]. In addition, we develop novel localization and online RIS calibration algorithms for cases with and without the knowledge of the underlying RIS amplitude model. The main contributions and novelty of our manuscript can be summarized as follows:

- **MCRB Analysis of Near-Field Localization under RIS Non-Idealities:** Employing the MCRB [41], [42] as a tool to assess the accuracy loss under model mismatch, we provide a simple expression to find the *pseudo-true parameter* for the considered scenario and derive the MCRB of the pseudo-true parameter and the lower bound (LB) of the true parameter. The MCRB analysis over a wide range of RIS model parameters reveals an order-of-magnitude localization performance degradation due to model misspecification at high SNRs, both in terms of the LB and the mismatched maximum-likelihood (MML) estimator [41]. In contrast, when the true phase control model is available, localization performance is relatively stable, for all considered model parameter settings.
- **Low-Complexity Near-Field Localization via Jacobi-Anger Expansion:** Building upon the ideas in our recent conference papers [27], [43], we develop a novel low-complexity near-field localization algorithm using Jacobi-Anger expansion, which enables decoupling of range, azimuth and elevation dimensions. The resulting algorithm, named approximated MML (AMML), avoids the costly 3-D search over the UE position by performing three 1-D searches and attains the corresponding theoretical limits.
- **Joint Localization and Online RIS Calibration:** Under the assumption of known RIS amplitude model with unknown parameters, we propose an efficient approximate maximum-likelihood (ML) (AML) algorithm for joint localization and online RIS calibration. The proposed approach iteratively updates the RIS model parameters based on an initial UE location estimate from the output of the model-unaware AMML method, and refines the UE location using the updated RIS model. The AML algorithm is shown to significantly outperform the AMML estimator at high SNRs (where degradation due to model mismatch is most evident), closing the performance gap with respect to the case with known model parameters, and converges quickly to the corresponding model-aware CRB in few iterations.

II. System Model

In this section, we describe the system geometry, present the signal model and the RIS model, and formulate the problem of interest.

A. Geometry and Signal Model

We consider an RIS-aided localization system (see Fig. 1) with a single-antenna BS, an M-element RIS, and a single-antenna UE having the following three-dimensional (3-D) locations: $\boldsymbol{p}_{\text{BS}}$ denotes the known BS location, $\boldsymbol{p}_{\text{RIS}} = [\text{x}_\text{R}\ \text{y}_\text{R}\ \text{z}_\text{R}]^\mathsf{T}$ is the known center of the RIS, $\boldsymbol{p}_m = [\text{x}_m\ \text{y}_m\ \text{z}_m]^\mathsf{T}$ represents the known location of the mth RIS element for $1 \leq m \leq M$, and $\overline{\boldsymbol{p}} = [\overline{\text{x}}\ \overline{\text{y}}\ \overline{\text{z}}]^\mathsf{T}$ is the unknown UE location. For convenience, following the notation given in [41], [44], we use $\overline{(\cdot)}$ for the true values of the parameters of interest throughout the manuscript.

In the considered setting, the BS broadcasts a narrowband signal s_t over T transmissions under the constraint of $\mathbb{E}\{|s_t|^2\} = E_s$. For simplicity, we assume that $s_t = \sqrt{E_s}$ for any t. Assuming LoS blockage [16], [28] and the absence of uncontrolled multipath[1], the signal received by the UE involves only reflections from the RIS and can be expressed at transmission t as

$$y_t = \overline{\alpha}\underbrace{\boldsymbol{a}^\mathsf{T}(\overline{\boldsymbol{p}})\text{diag}(\boldsymbol{w}_t)\boldsymbol{a}(\boldsymbol{p}_{\text{BS}})}_{\triangleq \boldsymbol{b}^\mathsf{T}(\overline{\boldsymbol{p}})\boldsymbol{w}_t} s_t + n_t\,, \tag{1}$$

where[2] $\overline{\alpha}$ is the unknown channel gain including the effects of path loss, directivity of the RIS elements and of the antennas of the BS and UE [16, Eq. (3)], and polarization

[1] In RIS-aided communications and localization, the uncontrolled multipath can usually be ignored [26], [33], [45] or treated as an extra additive disturbance [38] due to the spatial filtering capability of the RIS with tunable phase shifts, which makes the BS-RIS-UE path much stronger than the uncontrollable paths.

[2] The effect of mutual coupling (MC) between RIS elements can in principle be incorporated into the signal model (1) by replacing $\text{diag}(\boldsymbol{w}_t)$ by a non-diagonal matrix accounting for inter-element couplings [37]. To simplify the exposition and gain fundamental insights, the signal model is derived without MC, which is a common choice in the literature (e.g., [16], [26]–[28], [38]), and a possible extension including the effect of MC in future studies is mentioned in Sec. VII.

mismatch[3] [46, Ch. 1-11], $\boldsymbol{w}_t = [w_{t,1} \dots w_{t,M}]^\mathsf{T}$ is the RIS profile at transmission t, and n_t is uncorrelated zero-mean additive Gaussian noise with variance $N_0/2$ per real dimension. Moreover,

$$\boldsymbol{b}(\boldsymbol{p}) = \boldsymbol{a}(\boldsymbol{p}) \odot \boldsymbol{a}(\boldsymbol{p}_{\text{BS}}) \ , \tag{2}$$

where $\odot$ represents the Hadamard (element-wise) product and $\boldsymbol{a}(\boldsymbol{p})$ is the near-field RIS steering vector for a given position $\boldsymbol{p}$, defined as

$$[\boldsymbol{a}(\boldsymbol{p})]_m = \exp\left(-j\frac{2\pi}{\lambda}\left(\|\boldsymbol{p}-\boldsymbol{p}_m\| - \|\boldsymbol{p}-\boldsymbol{p}_{\text{RIS}}\|\right)\right) \tag{3}$$

for $m \in \{1,\dots,M\}$, in which λ denotes the signal wavelength and the RIS center $\boldsymbol{p}_{\text{RIS}}$ is chosen as the reference location [29], [31]. As the distance to the RIS becomes sufficiently large with respect to the RIS size, i.e., when $\|\boldsymbol{p}-\boldsymbol{p}_{\text{RIS}}\| \gg \|\boldsymbol{p}_m - \boldsymbol{p}_{\text{RIS}}\|$, the near-field steering vector in (3) reverts to its standard far-field counterpart as follows [47, Eq. (9)]

$$[\boldsymbol{a}(\boldsymbol{p})]_m \approx [\boldsymbol{a}(\vartheta,\varphi)]_m = \exp\left(-j(\boldsymbol{p}_m - \boldsymbol{p}_{\text{RIS}})^\mathsf{T}\boldsymbol{k}(\vartheta,\varphi)\right) \ , \tag{4}$$

where

$$\boldsymbol{k}(\vartheta,\varphi) = -\frac{2\pi}{\lambda}[\sin\vartheta\cos\varphi \ \ \sin\vartheta\sin\varphi \ \ \cos\vartheta]^\mathsf{T} \tag{5}$$

is the wavevector, $\vartheta \in [0, \pi/2]$ denote the elevation angle between the z-axis and $\boldsymbol{p}-\boldsymbol{p}_{\text{RIS}}$ (assuming the RIS orientation aligns with the x-y plane [27, Fig. 1]), and $\varphi \in [0, 2\pi]$ represent the azimuth angle between the projection of $\boldsymbol{p}-\boldsymbol{p}_{\text{RIS}}$ on the x-y plane and the x-axis, measured counter-clockwise.

For the considered geometry, the UE and the BS are assumed to be located in the Fresnel (radiative) near-field region with respect to the RIS, which corresponds to the interval [31], [48], [49]

$$0.62\sqrt{\frac{D^3}{\lambda}} \le d \le \frac{2D^2}{\lambda} \ , \tag{6}$$

where D is the RIS aperture size (i.e., the largest distance between any two RIS elements) and $d = \|\boldsymbol{p}-\boldsymbol{p}_{\text{RIS}}\|$ with $\boldsymbol{p}$ denoting the UE or BS location. Operating in the near-field enables us to localize the UE under LoS blockage by harnessing the *spherical wavefront* of the impinging signal at the UE over the BS-RIS-UE path [16], [29], [31]. As seen from the structure in (3), the unknown UE location $\overline{\boldsymbol{p}}$ can be directly estimated from the received signal in (1) by exploiting the phase shifts across the RIS elements (i.e., $m = 1,\dots,M$) over multiple observations (i.e., $t = 1,\dots,T$). In far-field, it is not possible to localize the UE with a single RIS under LoS blockage since the UE can only estimate the AoD from the RIS (the far-field steering vector in (4) depends only on the angles), which is not sufficient for localization. Note that the UE cannot extract any delay information in far-field in the considered setup due to narrowband transmission and asynchronism between the UE and the BS.

[3]Since the RIS aperture size is much smaller than the distances from the RIS to the BS and UE in the considered geometry, the channel gain appears as a global factor that has the same value for each RIS element [29, Eq. (3)].

B. Model for RIS Elements

Following the practical model in [35][4], we consider *phase-dependent amplitude variations* of the RIS elements given by

$$w_{t,m} = \beta(\theta_{t,m})e^{j\theta_{t,m}}, \tag{7}$$

with $\theta_{t,m} \in [-\pi,\pi)$ and $\beta(\theta_{t,m}) \in [0,1]$ denoting the phase shift[5] and the corresponding amplitude, respectively. In particular, $\beta(\theta_{t,m})$ is expressed as

$$\beta(\theta_{t,m}) = (1-\overline{\beta}_{\min})\left(\frac{\sin(\theta_{t,m}-\overline{\phi})+1}{2}\right)^{\overline{\kappa}} + \overline{\beta}_{\min}, \tag{8}$$

where $\overline{\beta}_{\min} \ge 0$, $\overline{\phi} \ge 0$, and $\overline{\kappa} \ge 0$ are the constants related to the specific circuit implementation [35]. To illustrate amplitude variations in (8), Fig. 2 plots $\beta(\theta)$ as a function of the applied phase shift θ for various values of $\overline{\beta}_{\min}$ when $\overline{\kappa} = 1.5$ and $\overline{\phi} = 0$. As seen from the figure, larger amplitude fluctuations occur as $\overline{\beta}_{\min}$ approaches 0. The resulting performance penalties in location estimation will be quantified through the MCRB analysis in Section III.

C. Problem Description

Given the observations y_t in (1) over T transmission instances, our goal is to derive theoretical performance bounds and develop low-complexity algorithms for estimating the position of the UE $\overline{\boldsymbol{p}}$ (and the channel gain $\overline{\boldsymbol{\alpha}}$ as an unknown nuisance parameter) under three different scenarios:

- *Scenario-I*: There is a mismatch between the assumption and the reality in this scenario. It is assumed that the amplitudes of the RIS elements are equal to 1 (which is equivalent to assuming $\overline{\beta}_{\min} = 1$ or $\overline{\kappa} = 0$); however, the *true model* is as in (7).
- *Scenario-II*: The *true model* in (7) is known, but the RIS related parameters, $\overline{\beta}_{\min}, \overline{\kappa}$, and $\overline{\phi}$, are assumed to be unknown.
- *Scenario-III*: Both the *true model* in (7) and the RIS related parameters, $\overline{\beta}_{\min}, \overline{\kappa}$, and $\overline{\phi}$, are known.

Note that the amplitude variations occur in the RIS elements through the RIS control model $w_{t,m}$ in (7), while the near-field effects manifest itself through the steering vector $\boldsymbol{a}(\boldsymbol{p})$ in

[4]The RIS phase-amplitude model in [35, Eq. (5)] covers a wide range of semiconductor devices employed in RIS implementation, such as a positive-intrinsic-negative (PIN) diode and a variable capacitance diode, and agrees well with the experimental results in the literature [35], [50]–[52]. It is possible to derive more accurate RIS phase-amplitude relations than in [35, Eq. (5)] using a generalized sheet transition conditions (GSTC) based model [53] instead of an equivalent circuit model. However, the goal of this paper is not to derive a perfectly accurate model of RIS element responses for all types of RISs (which is not practically possible), but rather to quantify the sensitivity of RIS-aided localization to deviations from the naive unit-amplitude model commonly used in the literature [16], [25]–[28], [30], [38] by adopting an already available, experimentally verified model with a closed-form phase-amplitude relation as in [35, Eq. (5)]. For experimental verification of [35, Eq. (5)] (corresponding to (8)), please see [50, Eq. (1)], [50, Fig. 5], [35, Eq. (4)], [35, Fig. 3] and [35, Fig. 4]. As will be discussed in Sec. III, the proposed MCRB analysis is generic and applicable to any RIS model with closed-form mapping between element phases and amplitudes.

[5]Given the near-optimal performance of RIS-aided systems using phase shifters with few quantization bits [18], [36], [54] and the availability of such low-resolution RIS phase shifters in practice [36], [51], we assume continuous phase shifts in our model. To see the effect of quantized amplitudes and phases of the received signals on localization accuracy in active RISs, which can sample the incoming signals unlike the passive RIS considered in this paper, the reader is referred to [55].

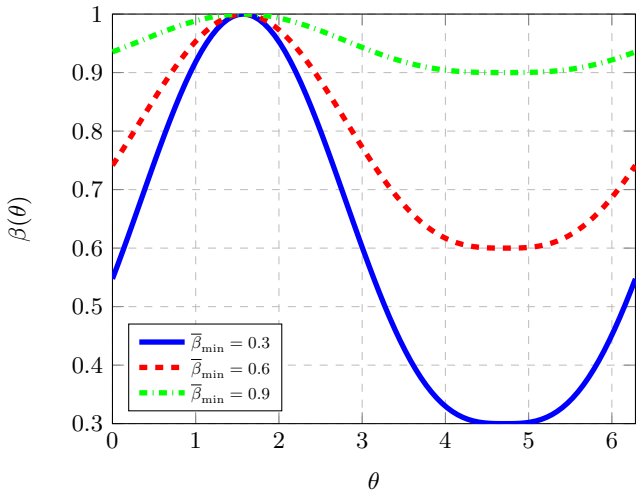

Fig. 2. $\beta(\theta)$ in (8) for three different values of $\overline{\beta}_{\min}$, when $\overline{\kappa} = 1.5$ and $\overline{\phi} = 0$.

(3). Hence, the considered scenarios differ in their knowledge about $w_{t,m}$, but they all consider the same steering vector $\boldsymbol{a}(\boldsymbol{p})$.

The motivation for considering Scenario I is to determine the conditions (regarding, e.g., SNR, RIS size, RIS model parameters $\overline{\beta}_{\min}, \overline{\kappa}$, and $\overline{\phi}$) under which the conventional unit-amplitude model can be employed for localization without significant performance degradation, when the true model is given by (7). On the other hand, we consider Scenario II to investigate how the effects of RIS amplitude variations on accuracy can be counteracted by designing powerful algorithms for localization and RIS model calibration, when the UE is aware of the true model in (7). Scenario III is mainly used for benchmarking purposes, i.e., to provide an upper bound on the performance of the algorithms developed under Scenario II.

To handle the different scenarios, the remainder of the manuscript is organized as follows. In Section III, the MCRB analysis of near-field localization under Scenario I is performed while Section IV focuses on the estimator design for Scenario I. Then, the localization algorithms and the theoretical bounds for Scenario II and Scenario III are presented in Section V. Finally, numerical examples for all the three scenarios are provided in Section VI.

III. Scenario-I: Misspecified Cramér-Rao Bound (MCRB) Analysis

In this scenario, we aim to quantify the localization performance loss due to the model mismatch resulting from the phase-dependent amplitude variations specified in (7). To that end, we will resort to the MCRB analysis [41], [44], [56], [57]. In the following, we first describe the *true model*, which corresponds to the realistic RIS response model in (7), and the *assumed model*, which is the ideal unit-amplitude RIS model commonly employed in the literature. Then, we provide theoretical background on the MCRB, propose a method to find the *pseudo-true parameter*, and derive the MCRB and the corresponding LB.

A. True and Assumed RIS Amplitude Models

1) True Model: The true parameter vector $\overline{\boldsymbol{\eta}}$ is given by $\overline{\boldsymbol{\eta}} \triangleq [\mathrm{Re}(\overline{\alpha})\, \mathrm{Im}(\overline{\alpha})\, \overline{\boldsymbol{p}}^{\mathsf{T}}]^{\mathsf{T}}$. We define μ_t as

$$\mu_t \triangleq \overline{\alpha} \sum_{m=1}^{M} [\boldsymbol{b}(\overline{\boldsymbol{p}})]_m w_{t,m} s_t \tag{9}$$

for $t = 1, \ldots, T$. Then, the probability density function (pdf) of the true observation, $p(\boldsymbol{y})$, can be expressed as

$$p(\boldsymbol{y}) = \left(\frac{1}{\pi N_0}\right)^T \exp\left(-\frac{1}{N_0} \|\boldsymbol{y} - \boldsymbol{\mu}\|^2\right), \tag{10}$$

where $\boldsymbol{y} \triangleq [y_1 \ \ldots \ y_T]^{\mathsf{T}}$ and $\boldsymbol{\mu} \triangleq [\mu_1 \ \ldots \ \mu_T]^{\mathsf{T}}$.

2) Assumed Model: In practice, the knowledge of the exact amplitude model in (8), which is hardware dependent, may not be available. In that case, the ideal model of $\beta(\theta_{t,m}) = 1$ can be used. For this *assumed model*, we represent $w_{t,m}$ as $\tilde{w}_{t,m}$, which is given by

$$\tilde{w}_{t,m} = e^{j\theta_{t,m}} \tag{11}$$

for any t and m. Therefore, the misspecified parametric pdf for $\boldsymbol{\eta} \triangleq [\mathrm{Re}(\alpha)\, \mathrm{Im}(\alpha)\, \boldsymbol{p}^{\mathsf{T}}]^{\mathsf{T}}$ under the assumed model, denoted by $\tilde{p}(\boldsymbol{y}|\boldsymbol{\eta})$, can be expressed as

$$\tilde{p}(\boldsymbol{y}|\boldsymbol{\eta}) = \left(\frac{1}{\pi N_0}\right)^T \exp\left(-\frac{1}{N_0} \|\boldsymbol{y} - \tilde{\boldsymbol{\mu}}(\boldsymbol{\eta})\|^2\right), \tag{12}$$

where $\tilde{\boldsymbol{\mu}}(\boldsymbol{\eta}) \triangleq [\tilde{\mu}_1(\boldsymbol{\eta}) \ \ldots \ \tilde{\mu}_T(\boldsymbol{\eta})]^{\mathsf{T}}$, and

$$\tilde{\mu}_t(\boldsymbol{\eta}) \triangleq \alpha \sum_{m=1}^{M} [\boldsymbol{b}(\boldsymbol{p})]_m \tilde{w}_{t,m} s_t \tag{13}$$

for $t = 1, \ldots, T$. It is noted that when $\overline{\beta}_{\min} = 1$ or $\overline{\kappa} = 0$, $p(\boldsymbol{y})$ and $\tilde{p}(\boldsymbol{y}|\overline{\boldsymbol{\eta}})$ coincide with each other for any $\boldsymbol{y}$.

B. MCRB Definition

We introduce the pseudo-true parameter [41], which minimizes the Kullback-Leibler (KL) divergence between the true pdf in (10) and the misspecified parametric pdf in (12); namely,

$$\boldsymbol{\eta}_0 = \underset{\boldsymbol{\eta} \in \mathbb{R}^5}{\arg\min}\, D\left(p(\boldsymbol{y}) \| \tilde{p}(\boldsymbol{y}|\boldsymbol{\eta})\right), \tag{14}$$

where $D\left(p(\boldsymbol{y}) \| \tilde{p}(\boldsymbol{y}|\boldsymbol{\eta})\right)$ denotes the KL divergence between the densities $p(\boldsymbol{y})$ and $\tilde{p}(\boldsymbol{y}|\boldsymbol{\eta})$.

Next, let $\hat{\boldsymbol{\eta}}(\boldsymbol{y})$ be a misspecified-unbiased (MS-unbiased) estimator of $\overline{\boldsymbol{\eta}}$, i.e., the mean of the estimator $\hat{\boldsymbol{\eta}}(\boldsymbol{y})$ under the true model is equal to $\boldsymbol{\eta}_0$. The MCRB is a lower bound for the covariance matrix of any MS-unbiased estimator of $\overline{\boldsymbol{\eta}}$, $\hat{\boldsymbol{\eta}}(\boldsymbol{y})$ [41], [42], [44]:

$$\mathbb{E}_p\{(\hat{\boldsymbol{\eta}}(\boldsymbol{y}) - \boldsymbol{\eta}_0)(\hat{\boldsymbol{\eta}}(\boldsymbol{y}) - \boldsymbol{\eta}_0)^{\mathsf{T}}\} \succeq \mathrm{MCRB}(\boldsymbol{\eta}_0), \tag{15}$$

where $\mathbb{E}_p\{\cdot\}$ denotes the expectation operator under the true model $p(\boldsymbol{y})$ and

$$\mathrm{MCRB}(\boldsymbol{\eta}_0) \triangleq \boldsymbol{A}_{\boldsymbol{\eta}_0}^{-1} \boldsymbol{B}_{\boldsymbol{\eta}_0} \boldsymbol{A}_{\boldsymbol{\eta}_0}^{-1}, \tag{16}$$

in which the (i,j)-th elements of the matrices $\boldsymbol{A}_{\boldsymbol{\eta}_0}$ and $\boldsymbol{B}_{\boldsymbol{\eta}_0}$ are calculated as

$$[\boldsymbol{A}_{\boldsymbol{\eta}_0}]_{ij} = \mathbb{E}_p\left\{\frac{\partial^2}{\partial \eta_i \partial \eta_j} \log \tilde{p}(\boldsymbol{y}|\boldsymbol{\eta})\Big|_{\boldsymbol{\eta}=\boldsymbol{\eta}_0}\right\}, \tag{17}$$

$$[\boldsymbol{B}_{\boldsymbol{\eta}_0}]_{ij} = \mathbb{E}_p \left\{ \frac{\partial}{\partial \eta_i} \log \tilde{p}(\boldsymbol{y}|\boldsymbol{\eta}) \frac{\partial}{\partial \eta_j} \log \tilde{p}(\boldsymbol{y}|\boldsymbol{\eta}) \Big|_{\boldsymbol{\eta}=\boldsymbol{\eta}_0} \right\}, \quad (18)$$

for $1 \leq i, j \leq 5$, with η_i denoting the ith element of $\boldsymbol{\eta}$.

Since the value of the pseudo-true parameter is generally not of interest, the MCRB is used to establish the LB of any MS-unbiased estimator with respect to the true parameter value [41]

$$\mathbb{E}_p\{(\hat{\boldsymbol{\eta}}(\boldsymbol{y}) - \overline{\boldsymbol{\eta}})(\hat{\boldsymbol{\eta}}(\boldsymbol{y}) - \overline{\boldsymbol{\eta}})^{\mathsf{T}}\} \succeq \mathrm{LB}(\boldsymbol{\eta}_0), \quad (19)$$

where

$$\mathrm{LB}(\boldsymbol{\eta}_0) \triangleq \mathrm{MCRB}(\boldsymbol{\eta}_0) + (\overline{\boldsymbol{\eta}} - \boldsymbol{\eta}_0)(\overline{\boldsymbol{\eta}} - \boldsymbol{\eta}_0)^{\mathsf{T}} . \quad (20)$$

The last term in (20) is a bias term; that is, $\mathrm{Bias}(\boldsymbol{\eta}_0) \triangleq (\overline{\boldsymbol{\eta}} - \boldsymbol{\eta}_0)(\overline{\boldsymbol{\eta}} - \boldsymbol{\eta}_0)^{\mathsf{T}}$, and it is independent of the SNR. Hence, as the SNR tends to infinity, the MCRB term goes to zero, and the bias term becomes a tight bound for the MSE of any MS-unbiased estimator.

C. MCRB Derivation for RIS-aided Localization

1) Determining the Pseudo-True Parameter: To derive the MCRB for estimating the UE position under mismatch between the amplitude models for the RIS elements, we should first calculate the $\boldsymbol{\eta}_0$ parameter in (14) for the system model described in Section II; that is, we should find the value of $\boldsymbol{\eta}$ that minimizes the KL divergence between $p(\boldsymbol{y})$ in (10) and $\tilde{p}(\boldsymbol{y}|\boldsymbol{\eta})$ in (12). The following lemma characterizes $\boldsymbol{\eta}_0$ for the considered system model.

Lemma 1. *The value of $\boldsymbol{\eta}$ that minimizes the KL divergence between $p(\boldsymbol{y})$ in* (10) *and $\tilde{p}(\boldsymbol{y}|\boldsymbol{\eta})$ in* (12) *can be expressed as*

$$\boldsymbol{\eta}_0 = \underset{\boldsymbol{\eta} \in \mathbb{R}^5}{\arg\min} \, \|\boldsymbol{\epsilon}(\boldsymbol{\eta})\| \quad (21)$$

where $\boldsymbol{\epsilon}(\boldsymbol{\eta}) \triangleq [\epsilon_1(\boldsymbol{\eta}) \ \ldots \ \epsilon_T(\boldsymbol{\eta})]^{\mathsf{T}}$ and $\epsilon_t(\boldsymbol{\eta}) \triangleq \mu_t - \tilde{\mu}_t(\boldsymbol{\eta})$ for $t = 1, \ldots, T$.

Proof. See Appendix A. □

Remark 1 (Applicability of Lemma 1 to Different RIS Models)**.** *The proof of Lemma 1 does not exploit the specific functional form of the adopted (true) RIS model in* (8) *and thus can be applied to different RIS models. Hence, Lemma 1 can be used to compute the MCRB and LB in* (20) *for any choice of the RIS element model $\beta(\theta_{t,m})$ in* (8) *by simply plugging the corresponding $w_{t,m}$ in* (7) *into the true model expressions in* (9) *and* (10)*.*

Lemma 1 states that the pseudo-true parameter minimizes the Euclidean distance between the noise-free observations under the true and assumed models.

Let $\gamma(\boldsymbol{\eta}) \triangleq \|\boldsymbol{\epsilon}(\boldsymbol{\eta})\| = \|\boldsymbol{\mu} - \tilde{\boldsymbol{\mu}}(\boldsymbol{\eta})\|$. It is noted from (9) and (13) that $\gamma(\boldsymbol{\eta})$ is non-convex with respect to $\boldsymbol{\eta}$; hence, it is challenging to solve (21) in its current form. Based on (12) and (13), we can re-write (21) as

$$(\boldsymbol{\alpha}_0, \boldsymbol{p}_0) = \underset{(\boldsymbol{\alpha}, \boldsymbol{p})}{\arg\min} \, \|\boldsymbol{\mu} - \alpha \, \boldsymbol{c}(\boldsymbol{p})\| , \quad (22)$$

where $[\boldsymbol{c}(\boldsymbol{p})]_t \triangleq \sum_{m=1}^{M} [\boldsymbol{b}(\boldsymbol{p})]_m \tilde{w}_{t,m} s_t$. The optimal complex-valued α for any given $\boldsymbol{p}$ can be expressed as

$$\alpha = \boldsymbol{c}(\boldsymbol{p})^{\dagger} \boldsymbol{\mu} , \quad (23)$$

where $\boldsymbol{X}^{\dagger} = (\boldsymbol{X}^{\mathsf{H}}\boldsymbol{X})^{-1}\boldsymbol{X}^{\mathsf{H}}$ denotes pseudo-inverse. Inserting (23) into (22), the problem can be reduced to a 3-D search as follows:

$$\boldsymbol{p}_0 = \underset{\boldsymbol{p}}{\arg\min} \left\| \boldsymbol{\Pi}^{\perp}_{\boldsymbol{c}(\boldsymbol{p})} \boldsymbol{\mu} \right\| , \quad (24)$$

where $\boldsymbol{\Pi}^{\perp}_{\boldsymbol{X}} = \mathbf{I} - \boldsymbol{\Pi}_{\boldsymbol{X}}$ and $\boldsymbol{\Pi}_{\boldsymbol{X}} = \boldsymbol{X}\boldsymbol{X}^{\dagger}$ denotes the orthogonal projection matrix onto the column space of $\boldsymbol{X}$. Therefore, $\boldsymbol{\eta}_0 = [\boldsymbol{\alpha}_0^{\mathsf{T}} \ \boldsymbol{p}_0^{\mathsf{T}}]^{\mathsf{T}}$ can be found by first performing a 3-D optimization as in (24), and then calculating α_0 via (23) and obtaining $\boldsymbol{\alpha}_0$ as $\boldsymbol{\alpha}_0 = [\mathrm{Re}(\alpha_0) \ \mathrm{Im}(\alpha_0)]^{\mathsf{T}}$.

Remark 2 (Initialization of (24))**.** *In order to determine the pseudo-true parameter or equivalently to find $\boldsymbol{p}_0$ in* (24)*, the true location $\overline{\boldsymbol{p}}$ can be used for initialization, which reduces the computational complexity of MCRB calculation significantly.*

Remark 3 (Special Cases of MCRB)**.** *As $\overline{\beta}_{\min}$ approaches* 1*, or $\overline{\kappa}$ approaches* 0*, the RIS amplitude $\beta(\theta_{t,m})$ in* (8) *converges to* 1*, implying that the phase-dependent amplitude variations model (true model) in* (7) *converges to the standard unit-amplitude model (assumed model) in* (11)*. In that case, the mismatch between the reality and the assumed model vanishes, which suggests that the pseudo-true parameter $\boldsymbol{\eta}_0$ in* (21) *approaches the true parameter $\overline{\boldsymbol{\eta}}$. As a result, the bias term in* (20) *disappears and the MCRB in* (16) *reverts to the classical Cramér-Rao bound (CRB) expression since $\boldsymbol{A}_{\boldsymbol{\eta}_0} = \boldsymbol{A}_{\overline{\boldsymbol{\eta}}} = -\boldsymbol{B}_{\boldsymbol{\eta}_0} = -\boldsymbol{B}_{\overline{\boldsymbol{\eta}}}$ [44].*

2) Deriving the MCRB: After finding $\boldsymbol{\eta}_0$, we compute the matrices $\boldsymbol{A}_{\boldsymbol{\eta}_0}$ from (17) and $\boldsymbol{B}_{\boldsymbol{\eta}_0}$ from (18) for evaluating the MCRB in (15). Based on the pdf expressions in (10)–(12), (17) becomes

$$[\boldsymbol{A}_{\boldsymbol{\eta}_0}]_{ij} = -\frac{1}{N_0} \left(\int \frac{\partial^2}{\partial \eta_i \partial \eta_j} \|\boldsymbol{y} - \tilde{\boldsymbol{\mu}}(\boldsymbol{\eta})\|^2 p(\boldsymbol{y}) \, d\boldsymbol{y} \right) \Big|_{\boldsymbol{\eta}=\boldsymbol{\eta}_0} \quad (25)$$

$$= -\frac{1}{N_0} \left(\sum_{t=1}^{T} \int \frac{\partial^2}{\partial \eta_i \partial \eta_j} |y_t - \tilde{\mu}_t(\boldsymbol{\eta})|^2 p(\boldsymbol{y}) \, d\boldsymbol{y} \right) \Big|_{\boldsymbol{\eta}=\boldsymbol{\eta}_0} \quad (26)$$

$$= -\frac{1}{N_0} \left(\sum_{t=1}^{T} \int \frac{\partial^2}{\partial \eta_i \partial \eta_j} |y_t - \tilde{\mu}_t(\boldsymbol{\eta})|^2 p(y_t) \, dy_t \right) \Big|_{\boldsymbol{\eta}=\boldsymbol{\eta}_0} \quad (27)$$

$$= \frac{2}{N_0} \mathrm{Re} \left\{ \sum_{t=1}^{T} \epsilon_t(\boldsymbol{\eta})^* \frac{\partial^2 \tilde{\mu}_t(\boldsymbol{\eta})}{\partial \eta_i \eta_j} - \frac{\partial \tilde{\mu}_t^*(\boldsymbol{\eta})}{\partial \eta_i} \frac{\partial \tilde{\mu}_t(\boldsymbol{\eta})}{\partial \eta_j} \right\} \Big|_{\boldsymbol{\eta}=\boldsymbol{\eta}_0} . \quad (28)$$

In addition, after some algebraic manipulation, the (i,j)th entry of matrix $\boldsymbol{B}_{\boldsymbol{\eta}_0}$ in (18) can be written as the sum of four terms as $[\boldsymbol{B}_{\boldsymbol{\eta}_0}]_{ij} = T_1 + T_2 + T_3 + T_4$, where

$$T_1 = \frac{1}{N_0^2} \left(\sum_{t=1}^{T} \frac{\partial \tilde{\mu}_t(\boldsymbol{\eta})}{\partial \eta_i} \epsilon_t(\boldsymbol{\eta})^* \right) \left(\sum_{l=1}^{T} \frac{\partial \tilde{\mu}_l(\boldsymbol{\eta})}{\partial \eta_j} \epsilon_l(\boldsymbol{\eta})^* \right) \Big|_{\boldsymbol{\eta}=\boldsymbol{\eta}_0}$$

$$T_2 = \left[\frac{1}{N_0^2} \left(\sum_{t=1}^{T} \frac{\partial \tilde{\mu}_t(\boldsymbol{\eta})}{\partial \eta_i} \epsilon_t(\boldsymbol{\eta})^* \right) \right.$$

$$\times \left(\sum_{l=1}^{T} \frac{\partial \tilde{\mu}_l^*(\boldsymbol{\eta})}{\partial \eta_j} \epsilon_l(\boldsymbol{\eta}) \right) + \frac{1}{N_0} \sum_{t=1}^{T} \frac{\partial \tilde{\mu}_t(\boldsymbol{\eta})}{\partial \eta_i} \frac{\partial \tilde{\mu}_t^*(\boldsymbol{\eta})}{\partial \eta_j} \Bigg] \Bigg|_{\boldsymbol{\eta}=\boldsymbol{\eta}_0}$$

$$T_3 = \frac{1}{N_0^2} \left(\sum_{t=1}^{T} \frac{\partial \tilde{\mu}_t^*(\boldsymbol{\eta})}{\partial \eta_i} \epsilon_t(\boldsymbol{\eta}) \right) \left(\sum_{t=1}^{T} \frac{\partial \tilde{\mu}_l^*(\boldsymbol{\eta})}{\partial \eta_j} \epsilon_l(\boldsymbol{\eta}) \right) \Bigg|_{\boldsymbol{\eta}=\boldsymbol{\eta}_0}$$

$$T_4 = \left[\frac{1}{N_0^2} \left(\sum_{t=1}^{T} \frac{\partial \tilde{\mu}_t^*(\boldsymbol{\eta})}{\partial \eta_i} \epsilon_t(\boldsymbol{\eta}) \right) \right.$$
$$\left. \times \left(\sum_{l=1}^{T} \frac{\partial \tilde{\mu}_l(\boldsymbol{\eta})}{\partial \eta_j} \epsilon_l(\boldsymbol{\eta})^* \right) + \frac{1}{N_0} \sum_{t=1}^{T} \frac{\partial \tilde{\mu}_t^*(\boldsymbol{\eta})}{\partial \eta_i} \frac{\partial \tilde{\mu}_t(\boldsymbol{\eta})}{\partial \eta_j} \right] \Bigg|_{\boldsymbol{\eta}=\boldsymbol{\eta}_0}.$$

Hence, $[\boldsymbol{A}_{\boldsymbol{\eta}_0}]_{ij}$ and $[\boldsymbol{B}_{\boldsymbol{\eta}_0}]_{ij}$ can be written in more compact forms as follows:

$$[\boldsymbol{A}_{\boldsymbol{\eta}_0}]_{ij} = \frac{2}{N_0} \mathrm{Re} \left\{ \boldsymbol{\epsilon}(\boldsymbol{\eta})^{\mathsf{H}} \frac{\partial^2 \tilde{\boldsymbol{\mu}}(\boldsymbol{\eta})}{\partial \eta_i \partial \eta_j} - \left(\frac{\partial \tilde{\boldsymbol{\mu}}(\boldsymbol{\eta})}{\partial \eta_i} \right)^{\mathsf{H}} \frac{\partial \tilde{\boldsymbol{\mu}}(\boldsymbol{\eta})}{\partial \eta_j} \right\} \Bigg|_{\boldsymbol{\eta}=\boldsymbol{\eta}_0} \tag{29}$$

$$[\boldsymbol{B}_{\boldsymbol{\eta}_0}]_{ij} = \frac{2}{N_0} \left[\frac{2}{N_0} \mathrm{Re} \left\{ \boldsymbol{\epsilon}(\boldsymbol{\eta})^{\mathsf{H}} \frac{\partial \tilde{\boldsymbol{\mu}}(\boldsymbol{\eta})}{\partial \eta_i} \right\} \mathrm{Re} \left\{ \boldsymbol{\epsilon}(\boldsymbol{\eta})^{\mathsf{H}} \frac{\partial \tilde{\boldsymbol{\mu}}(\boldsymbol{\eta})}{\partial \eta_j} \right\} \right.$$
$$\left. + \mathrm{Re} \left\{ \left(\frac{\partial \tilde{\boldsymbol{\mu}}(\boldsymbol{\eta})}{\partial \eta_i} \right)^{\mathsf{H}} \frac{\partial \tilde{\boldsymbol{\mu}}(\boldsymbol{\eta})}{\partial \eta_j} \right\} \right] \Bigg|_{\boldsymbol{\eta}=\boldsymbol{\eta}_0}, \tag{30}$$

where

$$\frac{\partial^2 \tilde{\boldsymbol{\mu}}(\boldsymbol{\eta})}{\partial \eta_i \partial \eta_j} \triangleq \left[\frac{\partial^2 \tilde{\mu}_1(\boldsymbol{\eta})}{\partial \eta_i \partial \eta_j} \cdots \frac{\partial^2 \tilde{\mu}_T(\boldsymbol{\eta})}{\partial \eta_i \partial \eta_j} \right]^{\mathsf{T}}. \tag{31}$$

Therefore, once we compute the first and the second derivatives of $\tilde{\mu}_t(\boldsymbol{\eta})$ with respect to $\boldsymbol{\eta}$, we can easily compute the matrices $\boldsymbol{A}_{\boldsymbol{\eta}_0}$ and $\boldsymbol{B}_{\boldsymbol{\eta}_0}$ as specified above. The derivatives are presented in Appendix E. Based on $\boldsymbol{A}_{\boldsymbol{\eta}_0}$ and $\boldsymbol{B}_{\boldsymbol{\eta}_0}$, the MCRB in (15) and the lower bound in (19) can be evaluated in a straightforward manner.

D. Localization Accuracy vs. Number of Transmissions

In order to illustrate the relationship between the localization accuracy and the number of transmissions, we analyze how the trace of the MCRB or the LB changes with respect to the number of transmissions, T. We consider two sets of observations for the same values of the true parameter vector $\overline{\boldsymbol{\eta}}$, the RIS size M, and the RIS related parameters $\beta_{\min}, \kappa, \phi$.

We prove that if repetitive RIS phase profiles are used, the MCRB and LB do not decay with $1/T$ whereas the CRB does. To be more specific, we state the following lemma.

Lemma 2. *For the k-th set of the observations, let the number of observations, the phase profile and the corresponding pseudo-true parameter be given by $T^{(k)}$, $\boldsymbol{\theta}^{(k)} = \{\theta_{t,m}^{(k)}\}_{\{t=1,m=1\}}^{\{T^{(k)},M\}}$, and $\boldsymbol{\eta}_0^{(k)}$, respectively, where $k \in \{1,2\}$.*

- *We assume that $T^{(2)} = KT^{(1)}$, where $K \in \mathbb{N}$.*
- *Moreover, for the phase profiles, for any $1 \leq m \leq M$, assume that*

$$\theta_{t,m}^{(2)} = \theta_{(t \bmod T^{(1)}),m}^{(1)} \tag{32}$$

where $\left(t \bmod T^{(1)}\right)$ denotes the remainder of the division of t by $T^{(1)}$.

Let $\mathrm{MCRB}\big(T^{(k)}, \boldsymbol{\eta}_0^{(k)}\big)$, $\mathrm{LB}\big(T^{(k)}, \boldsymbol{\eta}_0^{(k)}\big)$ and $\mathrm{CRB}\big(T^{(k)}\big)$ denote the corresponding MCRB, LB and CRB for the k-th set of observations. Then,

$$\frac{1}{K} < \frac{\mathrm{Tr}\left\{\mathrm{MCRB}\big(T^{(2)}, \boldsymbol{\eta}_0^{(2)}\big)\right\}}{\mathrm{Tr}\left\{\mathrm{MCRB}\big(T^{(1)}, \boldsymbol{\eta}_0^{(1)}\big)\right\}} < 1,$$
$$\frac{1}{K} < \frac{\mathrm{Tr}\left\{\mathrm{LB}\big(T^{(2)}, \boldsymbol{\eta}_0^{(2)}\big)\right\}}{\mathrm{Tr}\left\{\mathrm{LB}\big(T^{(1)}, \boldsymbol{\eta}_0^{(1)}\big)\right\}} < 1 \text{ and } \frac{\mathrm{Tr}\left\{\mathrm{CRB}\big(T^{(2)}\big)\right\}}{\mathrm{Tr}\left\{\mathrm{CRB}\big(T^{(1)}\big)\right\}} = \frac{1}{K}.$$

Proof. See Appendix B. □

Lemma 2 reveals that the trace of the CRB decays with $1/T$ while that of the MCRB or LB decays slower than $1/T$ due to model misspecification.

IV. Scenario-I: Mismatched Estimator

In this section, we focus on estimator design for Scenario-I. First, we derive the plain MML estimator, which entails computationally prohibitive high-dimensional non-convex optimization. To circumvent this, we then propose a low-complexity estimator capitalizing on the Jacobi-Anger expansion, which reduces the problem to a series of line searches over range, azimuth, and elevation domains.

A. Mismatched Maximum Likelihood (MML) Estimator

Given the pdf of the assumed model in (12), the MML estimator is given by [41]

$$\hat{\boldsymbol{\eta}}_{\mathrm{MML}}(\boldsymbol{y}) = \underset{\boldsymbol{\eta} \in \mathbb{R}^5}{\arg\max} \log \tilde{p}(\boldsymbol{y}|\boldsymbol{\eta}). \tag{33}$$

Under some regularity conditions, it can be shown that $\hat{\boldsymbol{\eta}}_{\mathrm{MML}}(\boldsymbol{y})$ is asymptotically MS-unbiased and its error covariance matrix is asymptotically equal to the $\mathrm{MCRB}(\boldsymbol{\eta}_0)$ [41, Thm. 2]. Hence, the covariance matrix of the MML estimator is asymptotically tight to the MCRB.

From (12) and (33), the MML estimator based on the received signal $\boldsymbol{y}$ in (1) can be expressed as

$$\hat{\boldsymbol{\eta}}_{\mathrm{MML}}(\boldsymbol{y}) = \underset{\boldsymbol{\eta} \in \mathbb{R}^5}{\arg\max} \log \tilde{p}(\boldsymbol{y}|\boldsymbol{\eta}) = \underset{\boldsymbol{\eta} \in \mathbb{R}^5}{\arg\min} \left\| \boldsymbol{y} - \tilde{\boldsymbol{\mu}}(\boldsymbol{\eta}) \right\|. \tag{34}$$

Since this problem is in the same form as in (21), it can be reduced to a 3-D optimization problem as discussed in Section III-C. In order to solve the resulting problem, initialization can be very critical as we are faced with a non-convex optimization problem. During the estimation process, we do not have access to the true position $\overline{\boldsymbol{p}}$. Hence, we cannot use the true position vector $\overline{\boldsymbol{p}}$ for the initialization. If an arbitrarily chosen position vector is used for the initialization, the global optimal solution of (33) cannot always be obtained. To find a remedy for this issue, we next propose an approximated version of the MML estimator in (34), namely, the approximate mismatched maximum likelihood (AMML) estimator. Additionally, to reduce the complexity of the proposed algorithm, we propose a Jacobi-Anger expansion based approach when the number of transmissions is sufficiently large [27], [43], [58].

B. AMML Estimator

Let us first re-write $\tilde{\boldsymbol{\mu}}(\boldsymbol{\eta})$ in (13) using (2) as

$$\tilde{\boldsymbol{\mu}}(\boldsymbol{\eta}) = \alpha \underbrace{\begin{bmatrix} (\tilde{\boldsymbol{w}}_1 \odot \boldsymbol{a}(\boldsymbol{p}_{\text{BS}}))^{\mathsf{T}} \\ \vdots \\ (\tilde{\boldsymbol{w}}_T \odot \boldsymbol{a}(\boldsymbol{p}_{\text{BS}}))^{\mathsf{T}} \end{bmatrix}}_{\triangleq \boldsymbol{Q} \in \mathbb{C}^{T \times M}} \boldsymbol{a}(\boldsymbol{p}) \sqrt{E_s} \ , = \alpha \boldsymbol{Q} \boldsymbol{a}(\boldsymbol{p}) \sqrt{E_s} \ , \tag{35}$$

where $\tilde{\boldsymbol{w}}_t \triangleq [\tilde{w}_{t,1} \ \dots \ \tilde{w}_{t,M}]^{\mathsf{T}}$ and $s_t = \sqrt{E_s}$ for any t. Inserting (35) into (34), the MML estimator becomes

$$(\widehat{\alpha}, \widehat{d}, \widehat{\vartheta}, \widehat{\varphi}) = \underset{\alpha, d, \vartheta, \varphi}{\arg\min} \left\| \boldsymbol{y} - \alpha \, \boldsymbol{Q} \boldsymbol{a} \left(\boldsymbol{p}(d, \vartheta, \varphi) \right) \sqrt{E_s} \right\| \ , \tag{36}$$

where

$$\boldsymbol{p}(d, \vartheta, \varphi) \triangleq \boldsymbol{p}_{\text{RIS}} + d \left[\sin\vartheta \cos\varphi \ \ \sin\vartheta \sin\varphi \ \ \cos\vartheta \right]^{\mathsf{T}} \tag{37}$$

denotes the position vector with respect to $\boldsymbol{p}_{\text{RIS}}$ in spherical coordinates according to the definitions after (5). Since $\widehat{\alpha}$ can be obtained in closed-form as a function of the other unknowns as in (23), (36) can be solved via 3-D optimization. In the following, we describe the steps to solve (36) in an efficient manner.

1) Approximation of Near-Field as Far-Field for Initial Azimuth and Elevation Estimation: To avoid 3-D search in (36), we approximate the near-field steering vector as its far-field counterpart via (4):

$$[\boldsymbol{a}(\boldsymbol{p})]_m \approx [\boldsymbol{a}(\vartheta, \varphi)]_m \ , \tag{38}$$

which reduces (36) to

$$(\widehat{\alpha}, \widehat{\vartheta}, \widehat{\varphi}) = \underset{\alpha, \vartheta, \varphi}{\arg\min} \left\| \boldsymbol{y} - \alpha \, \boldsymbol{Q} \boldsymbol{a}(\vartheta, \varphi) \sqrt{E_s} \right\| \ . \tag{39}$$

Similar to (23), $\widehat{\alpha}$ can be estimated in closed-form as a function of ϑ and φ in (39), leading to

$$(\widehat{\vartheta}, \widehat{\varphi}) = \underset{\substack{\vartheta \in [0, \, \pi/2] \\ \varphi \in [0, \, 2\pi]}}{\arg\min} \left\| \boldsymbol{\Pi}^{\perp}_{\boldsymbol{Q}\boldsymbol{a}(\vartheta, \varphi)} \boldsymbol{y} \right\| \ . \tag{40}$$

In (40), initial azimuth and elevation estimates can be found by conducting 2-D search over ϑ and φ.

2) Switching Back to Near-Field for Location Estimation: Starting from the initial estimates $\widehat{\vartheta}$ and $\widehat{\varphi}$ in the approximated MML estimator (40), location estimation can be performed by switching back to the original MML estimator (36) based on the near-field model via the following alternating iterations.

- *Update d:* Given $\widehat{\vartheta}$ and $\widehat{\varphi}$, we estimate distance d in (36) as

$$(\widehat{\alpha}, \widehat{d}) = \underset{\alpha, d}{\arg\min} \left\| \boldsymbol{y} - \alpha \, \boldsymbol{Q} \boldsymbol{a} \big(\boldsymbol{p}(d, \widehat{\vartheta}, \widehat{\varphi}) \big) \sqrt{E_s} \right\| \ . \tag{41}$$

  Similar to the solution of (39), distance can be estimated from (41) via

$$\widehat{d} = \underset{d \in (0, d_{\max})}{\arg\min} \left\| \boldsymbol{\Pi}^{\perp}_{\boldsymbol{Q}\boldsymbol{a}(\boldsymbol{p}(d, \widehat{\vartheta}, \widehat{\varphi}))} \boldsymbol{y} \right\| \ , \tag{42}$$

  which entails a simple line search for a given maximum distance $d_{\max}$ imposed by near-field conditions in (6).

- *Update ϑ and φ:* Given $\widehat{d}$ from (42), azimuth and elevation estimates can be updated in (36) via

$$(\widehat{\alpha}, \widehat{\vartheta}, \widehat{\varphi}) = \underset{\alpha, \vartheta, \varphi}{\arg\min} \left\| \boldsymbol{y} - \alpha \, \boldsymbol{Q} \boldsymbol{a} \big(\boldsymbol{p}(\widehat{d}, \vartheta, \varphi) \big) \sqrt{E_s} \right\| \ , \tag{43}$$

  leading to

$$(\widehat{\vartheta}, \widehat{\varphi}) = \underset{\substack{\vartheta \in [0, \, \pi/2] \\ \varphi \in [0, \, 2\pi]}}{\arg\min} \left\| \boldsymbol{\Pi}^{\perp}_{\boldsymbol{Q}\boldsymbol{a}(\boldsymbol{p}(\widehat{d}, \vartheta, \varphi))} \boldsymbol{y} \right\| \ . \tag{44}$$

After a predetermined number of iterations $I_{\max}$, the resulting estimates of elevation, azimuth and distance from (42) and (44) are inserted into $\boldsymbol{p}(\widehat{d}, \widehat{\vartheta}, \widehat{\varphi})$ in (37) to find the AMML estimate for the UE location.

To further reduce the complexity, we next propose a Jacobi-Anger expansion based estimator that avoids 2-D searches in (40) and (44) for large number of transmissions T.

C. Jacobi-Anger Expansion Based AMML Estimator for Large Number of Transmissions

In this part, we develop a low-complexity multi-step approach to estimate the UE position in the MML estimator (36) by leveraging the Jacobi-Anger expansion [59], as detailed in the following.

1) Jacobi-Anger Approximation to Decouple Azimuth and Elevation Parameters in Far-Field: Similar to Sec. IV-B, we begin by invoking the far-field approximation in (4) and considering the resulting approximated estimator in (39). Using (5), the far-field steering vector in (4) can be expressed as

$$[\boldsymbol{a}(\vartheta, \varphi)]_m = \exp\left(j \frac{2\pi}{\lambda} q_m \sin(\vartheta) \cos(\varphi - \psi_m) \right) \ , \tag{45}$$

where $q_m = \|\boldsymbol{p}_m - \boldsymbol{p}_{\text{RIS}}\|$ and ψ_m is the angle between $\boldsymbol{p}_m - \boldsymbol{p}_{\text{RIS}}$ and the x-axis, i.e.,

$$\boldsymbol{p}_m - \boldsymbol{p}_{\text{RIS}} = q_m [\cos(\psi_m) \ \ \sin(\psi_m) \ \ 0]^{\mathsf{T}} \ . \tag{46}$$

By employing the Jacobi-Anger expansion, $[\boldsymbol{a}(\vartheta, \varphi)]_m$ in (45) can be expressed as [59, Eq. (17.1.7)]

$$[\boldsymbol{a}(\vartheta, \varphi)]_m = \sum_{n=-\infty}^{\infty} j^n J_n \left(\frac{2\pi}{\lambda} q_m \sin\vartheta \right) e^{jn(\varphi - \psi_m)} \ , \tag{47}$$

where $J_n(\cdot)$ is the nth order Bessel function of the first kind. As $|J_n(\cdot)|$ decays to 0 as $|n|$ increases, by neglecting the terms with $|n| > N$, for some $N \in \mathbb{N}$, (47) can be approximated by [58]

$$[\boldsymbol{a}(\vartheta, \varphi)]_m \approx \sum_{n=-N}^{N} j^n J_n \left(\frac{2\pi}{\lambda} q_m \sin\vartheta \right) e^{jn(\varphi - \psi_m)} \ , \tag{48}$$

where

$$N > \frac{2\pi}{\lambda} q_{\max} \sin\vartheta \tag{49}$$

enables sufficient precision for high-quality approximation [58], with $q_{\max}$ denoting the maximum distance of any RIS element from the RIS centre. To provide a compact expression for (48), we define $\boldsymbol{g}_m(\vartheta) \in \mathbb{C}^{(2N+1)\times 1}$ and $\boldsymbol{h}(\varphi) \in \mathbb{C}^{(2N+1)\times 1}$ as

$$[\boldsymbol{g}_m(\vartheta)]_n = j^n J_n \left(\frac{2\pi}{\lambda} q_m \sin\vartheta \right) e^{-jn\psi_m} \ , \tag{50}$$

$$[\boldsymbol{h}(\varphi)]_n = e^{jn\varphi} \tag{51}$$

for $n \in \{-N, \ldots, N\}$. Then, inserting (50) and (51) into (48) yields

$$\boldsymbol{a}(\vartheta, \varphi) \approx \boldsymbol{G}^{\mathsf{T}}(\vartheta)\boldsymbol{h}(\varphi), \tag{52}$$

where

$$\boldsymbol{G}(\vartheta) = [\boldsymbol{g}_1(\vartheta) \ \ldots \ \boldsymbol{g}_M(\vartheta)] \in \mathbb{C}^{(2N+1)\times M}. \tag{53}$$

As seen from (52), the proposed Jacobi-Anger expansion of the far-field RIS steering vector in (45) enables decoupling azimuth and elevation parameters in a matrix-vector multiplication form.

2) Azimuth and Elevation Estimation via Unstructured ML: We can now exploit the structure in (52) to recast the MML estimator in (39) as

$$(\widehat{\alpha}, \widehat{\vartheta}, \widehat{\varphi}) = \underset{\alpha,\vartheta,\varphi}{\arg\min} \left\| \boldsymbol{y} - \alpha\, \boldsymbol{Q}\boldsymbol{G}^{\mathsf{T}}(\vartheta)\boldsymbol{h}(\varphi)\sqrt{E_s} \right\| . \tag{54}$$

To enable decoupled estimation of azimuth and elevation parameters in (54), we resort to unstructured ML techniques [60]. To this end, let

$$\boldsymbol{f} \triangleq \alpha\, \boldsymbol{h}(\varphi)\sqrt{E_s} \in \mathbb{C}^{(2N+1)\times 1} \tag{55}$$

denote the unstructured vector where the dependency on α and φ is dropped. Substituting (55) into (54) yields the unstructured ML optimization problem:

$$(\widehat{\boldsymbol{f}}, \widehat{\vartheta}) = \underset{\boldsymbol{f},\vartheta}{\arg\min} \left\| \boldsymbol{y} - \boldsymbol{Q}\boldsymbol{G}^{\mathsf{T}}(\vartheta)\boldsymbol{f} \right\| . \tag{56}$$

In (56), $\widehat{\boldsymbol{f}}$ can be readily obtained as a function of ϑ

$$\widehat{\boldsymbol{f}} = \left(\boldsymbol{Q}\boldsymbol{G}^{\mathsf{T}}(\vartheta)\right)^{\dagger} \boldsymbol{y} \tag{57}$$

under the condition $T \geq 2N+1$, noting that $\boldsymbol{Q}\boldsymbol{G}^{\mathsf{T}}(\vartheta) \in \mathbb{C}^{T\times(2N+1)}$. By plugging (57) back into (56), elevation can be estimated via a simple line search:

$$\widehat{\vartheta} = \underset{\vartheta\in[0,\,\pi/2]}{\arg\min} \left\| \boldsymbol{\Pi}^{\perp}_{\boldsymbol{Q}\boldsymbol{G}^{\mathsf{T}}(\vartheta)}\boldsymbol{y} \right\| . \tag{58}$$

Using the estimated elevation $\widehat{\vartheta}$ in (58), the ML problem in (54) can be recast as

$$(\widehat{\alpha}, \widehat{\varphi}) = \underset{\alpha,\varphi}{\arg\min} \left\| \boldsymbol{y} - \alpha\, \boldsymbol{Q}\boldsymbol{G}^{\mathsf{T}}(\widehat{\vartheta})\boldsymbol{h}(\varphi)\sqrt{E_s} \right\| , \tag{59}$$

where the task of azimuth estimation boils down to a line search:

$$\widehat{\varphi} = \underset{\varphi\in[0,\,2\pi]}{\arg\min} \left\| \boldsymbol{\Pi}^{\perp}_{\boldsymbol{Q}\boldsymbol{G}^{\mathsf{T}}(\widehat{\vartheta})\boldsymbol{h}(\varphi)}\boldsymbol{y} \right\| . \tag{60}$$

3) Distance Estimation Using the Near-Field Model: Having estimated the elevation and azimuth in (58) and (60), respectively, using the far-field approximation, we can now switch back to the original near-field based MML estimator in (36) and retrieve distance information via (42).

D. Summary of AMML Based Algorithm

In Sec. IV-B and Sec. IV-C, we propose two approaches to implement the MML estimator in (34). The approach in Sec. IV-B can be used for any number of transmissions T, while the one in Sec. IV-C represents a low-complexity alternative that can be employed for $T \geq T_{\text{thr}} = 2N+1$ due to the condition imposed in (57). Here, N can be set according to (49). Therefore, we can decide on the preferred approach depending on whether $T \geq T_{\text{thr}}$ holds. The entire algorithm is summarized in Algorithm 1.

Algorithm 1 AMML Algorithm for RIS-aided Near-Field Localization via Jacobi-Anger Expansion

Input: Observation $\boldsymbol{y}$ in (1), T_{thr}, $I_{\max}$.
Output: Location estimate $\widehat{\boldsymbol{p}}$.
if $T \geq T_{\text{thr}}$ **then**
  Estimate the elevation $\widehat{\vartheta}$ by solving (58).
  Using $\widehat{\vartheta}$, estimate the azimuth $\widehat{\varphi}$ by solving (60).
  Using $\widehat{\vartheta}$ and $\widehat{\varphi}$, estimate the distance $\widehat{d}$ by solving (42).
else
  Find the initial estimates $\widehat{\vartheta}$ and $\widehat{\varphi}$ by solving (40).
  Set $i = 0$.
  while the objective function in (36) does not converge and $i < I_{\max}$ **do**
    Update $\widehat{d}$ by solving (42).
    Update $\widehat{\vartheta}$ and $\widehat{\varphi}$ by solving (44).
    Set $i = i + 1$.
  end while
end if
Compute the location estimate via (37) as $\widehat{\boldsymbol{p}} = \boldsymbol{p}(\widehat{d}, \widehat{\vartheta}, \widehat{\varphi})$.

E. Complexity and Convergence of Algorithm 1

To evaluate the computational complexity of Algorithm 1, suppose that the search intervals for distance, azimuth and elevation are discretized into grids of size K each. We assume that $K, M > T$, which is reasonable given the large RIS size and a fine search granularity required for high-quality estimates. As shown in detail in Appendix C, the overall cost of Algorithm 1 for $T < T_{\text{thr}} = 2N+1$ and $T \geq T_{\text{thr}}$ is given by $\mathcal{O}(TK^2M)$ and $\mathcal{O}\left(TM(2N+1)K\right)$, respectively. For $T \geq T_{\text{thr}}$, we have $K > T \geq 2N+1$, leading to $TM(2N+1)K \leq TK^2M$. Thus, it can be concluded that, when T is sufficiently large, by using the Jacobi-Anger expansion based estimator in Sec. IV-C, we decrease the computational complexity. Thus, for $T \geq 2N+1$ where N is sufficiently large (e.g., (49)) to provide a good approximation in (48), the Jacobi-Anger based approach can be employed to reduce the computational burden.

Regarding the convergence of Algorithm 1, it follows from [61, Prop. 1] that if the solutions to (42) and (44) are unique, then Algorithm 1 converges to a stationary point of the original MML estimation problem in (36). Note that the uniqueness of the solutions to (42) and (44) can be achieved with high probability using random RIS phase profiles [38, Sec. IV-B].

Next, we analyze how the performance bounds and the estimator structures are affected when the true RIS amplitude model given in (7) is known.

V. Scenario-II & Scenario-III: RIS-aided Localization Under Known RIS Amplitude Model

In this section, we investigate RIS-aided localization under Scenario-II and Scenario-III, where the UE is assumed to be aware of the RIS amplitude model in (7).

A. Scenario-II: Known RIS Amplitude Model with Unknown Parameters

In this scenario, in order to parameterize the unknown system parameters, we will use $\boldsymbol{\eta} = [\mathrm{Re}(\alpha)\, \mathrm{Im}(\alpha)\, \boldsymbol{p}^{\mathsf{T}}\, \beta_{\min}\, \kappa\, \phi]^{\mathsf{T}}$, which consists of both the channel parameters and the RIS model parameters. Then, by [27, Eq. 9], the Fisher Information matrix (FIM), $\boldsymbol{J}(\boldsymbol{\eta}) \in \mathbb{R}^{8\times 8}$, can be expressed as

$$\boldsymbol{J}(\boldsymbol{\eta}) = \frac{2}{N_0}\mathrm{Re}\left\{\left(\frac{\partial \boldsymbol{\mu}}{\partial \boldsymbol{\eta}}\right)^{\mathsf{H}} \frac{\partial \boldsymbol{\mu}}{\partial \boldsymbol{\eta}}\right\}. \tag{61}$$

In order to compute the derivatives of $\boldsymbol{\mu}$ with respect to the first five entries of $\boldsymbol{\eta}$, we can use the derivatives given in Appendix E by replacing the $\tilde{w}_{t,m}$ terms with $w_{t,m}$. For the last three entries of $\boldsymbol{\eta}$, i.e., for the RIS related parameters, the derivatives used in (61) are provided in Appendix F.

After obtaining the FIM, by computing $\mathrm{Tr}\{\boldsymbol{J}^{-1}(\boldsymbol{\eta})\}_{3:5,3:5}$, we can obtain the CRB for estimating the UE position. Moreover, the ML estimator can be stated as

$$\hat{\boldsymbol{\eta}}_{\mathrm{ML}}(\boldsymbol{y}) = \underset{\boldsymbol{\eta}\in\mathbb{R}^8}{\arg\max} \log p(\boldsymbol{y}). \tag{62}$$

As discussed in Section III-C, the estimate for $\overline{\alpha}$ can uniquely be determined for given estimates of $\overline{\boldsymbol{p}}$, $\overline{\beta}_{\min}$, $\overline{\kappa}$, and $\overline{\phi}$. That is, this problem can be reduced to a 6-dimensional optimization problem. Similar to the mismatched scenario (Scenario-I), the initialization is an important issue for this scenario, as well. For practical implementations, we propose an approximate version of the ML estimator, called the approximate maximum likelihood (AML) estimator, in the next section.

B. Scenario-II: AML Estimator

In this part, our goal is to solve the problem of *joint localization and online RIS calibration* in (62), which involves estimating the UE location $\overline{\boldsymbol{p}}$ and the RIS model parameters $\overline{\beta}_{\min}$, $\overline{\kappa}$, and $\overline{\phi}$ simultaneously. To accomplish this in an efficient manner, we propose a low-complexity estimator as an alternative to the high-dimensional non-convex optimization in (62).

Let us write the observations in (1) in a vector form as

$$\boldsymbol{y} = \bar{\alpha}\, \boldsymbol{W}^{\mathsf{T}}(\overline{\boldsymbol{\zeta}})\boldsymbol{b}(\overline{\boldsymbol{p}})\sqrt{E_s} + \boldsymbol{n}, \tag{63}$$

where $\boldsymbol{W}(\overline{\boldsymbol{\zeta}}) = [\boldsymbol{w}_1(\overline{\boldsymbol{\zeta}}) \ \ldots \ \boldsymbol{w}_T(\overline{\boldsymbol{\zeta}})] \in \mathbb{C}^{M\times T}$ is the matrix of RIS profiles as a function of the parameters $\overline{\boldsymbol{\zeta}} = [\overline{\beta}_{\min}\ \overline{\kappa}\ \overline{\phi}]^{\mathsf{T}}$ of the RIS amplitude model in (7) and (8), and $\boldsymbol{n} = [n_1 \ldots n_T]^{\mathsf{T}}$ is the additive noise vector. From (7) and (8), $\boldsymbol{W}(\overline{\boldsymbol{\zeta}})$ can be expressed as

$$\boldsymbol{W}(\overline{\boldsymbol{\zeta}}) = \left(\overline{\beta}_{\min}\boldsymbol{\Gamma}_1(\overline{\kappa},\overline{\phi}) + \boldsymbol{\Gamma}_2(\overline{\kappa},\overline{\phi})\right) \odot e^{j\boldsymbol{\Theta}}, \tag{64}$$

where $\boldsymbol{\Theta} \in \mathbb{R}^{M\times T}$ denotes the RIS phase shifts with $[\boldsymbol{\Theta}]_{m,t} = \theta_{m,t}$,

$$\boldsymbol{\Gamma}_1(\overline{\kappa},\overline{\phi}) \triangleq \mathbf{1}_M\mathbf{1}_T^{\mathsf{T}} - \left(\frac{\sin(\boldsymbol{\Theta}-\overline{\phi})+1}{2}\right)^{\overline{\kappa}}, \tag{65}$$

$$\boldsymbol{\Gamma}_2(\overline{\kappa},\overline{\phi}) \triangleq \left(\frac{\sin(\boldsymbol{\Theta}-\overline{\phi})+1}{2}\right)^{\overline{\kappa}}, \tag{66}$$

$\mathbf{1}_M$ is an all-ones vector of size M, and $\sin(\cdot)$ and $(\cdot)^{\overline{\kappa}}$ operations are element-wise. Plugging $\boldsymbol{b}(\overline{\boldsymbol{p}}) = \boldsymbol{a}(\overline{\boldsymbol{p}}) \odot \boldsymbol{a}(\boldsymbol{p}_{\mathrm{BS}})$ and (64) into (63) yields

$$\boldsymbol{y} = \overline{\alpha}\left(\overline{\beta}_{\min}\widetilde{\boldsymbol{\Gamma}}_1(\overline{\kappa},\overline{\phi}) + \widetilde{\boldsymbol{\Gamma}}_2(\overline{\kappa},\overline{\phi})\right)^{\mathsf{T}}\boldsymbol{a}(\overline{\boldsymbol{p}})\sqrt{E_s} + \boldsymbol{n}, \tag{67}$$

where

$$\begin{aligned}\widetilde{\boldsymbol{\Gamma}}_1(\overline{\kappa},\overline{\phi}) &\triangleq \boldsymbol{\Gamma}_1(\overline{\kappa},\overline{\phi}) \odot e^{j\boldsymbol{\Theta}} \odot \boldsymbol{a}(\boldsymbol{p}_{\mathrm{BS}})\mathbf{1}_T^{\mathsf{T}}, \\ \widetilde{\boldsymbol{\Gamma}}_2(\overline{\kappa},\overline{\phi}) &\triangleq \boldsymbol{\Gamma}_2(\overline{\kappa},\overline{\phi}) \odot e^{j\boldsymbol{\Theta}} \odot \boldsymbol{a}(\boldsymbol{p}_{\mathrm{BS}})\mathbf{1}_T^{\mathsf{T}}.\end{aligned} \tag{68}$$

The ML estimator corresponding to the observation model in (67) is given by

$$\min_{\alpha,\boldsymbol{p},\boldsymbol{\zeta}} \left\|\boldsymbol{y} - \alpha\left(\beta_{\min}\widetilde{\boldsymbol{\Gamma}}_1(\kappa,\phi) + \widetilde{\boldsymbol{\Gamma}}_2(\kappa,\phi)\right)^{\mathsf{T}}\boldsymbol{a}(\boldsymbol{p})\sqrt{E_s}\right\|^2. \tag{69}$$

To solve the ML optimization problem in (69), we now propose a three-step procedure consisting of location initialization, online RIS calibration and location refinement.

1) Step 0: Initialization of UE Location: First, by assuming $\beta_{\min} = 1$, the initial location estimate $\widehat{\boldsymbol{p}}$ is obtained by using the Jacobi-Anger expansion based algorithm in Algorithm 1. Inserting $\widehat{\boldsymbol{p}}$ into the ML estimator in (69), the optimization problem becomes

$$\min_{\alpha,\boldsymbol{\zeta}} \left\|\boldsymbol{y} - \alpha\left(\beta_{\min}\widetilde{\boldsymbol{\Gamma}}_1(\kappa,\phi) + \widetilde{\boldsymbol{\Gamma}}_2(\kappa,\phi)\right)^{\mathsf{T}}\boldsymbol{a}(\widehat{\boldsymbol{p}})\sqrt{E_s}\right\|^2. \tag{70}$$

2) Step 1: Online RIS Calibration: As noted from (70), $\overline{\alpha}$ and $\overline{\beta}_{\min}$ can now be estimated in closed-from as a function of the remaining unknown parameters, while the estimates of $\overline{\kappa}$ and $\overline{\phi}$ can be found via a 2-D search. This motivates an alternating optimization algorithm where we alternate among updates of α, $\beta_{\min}$, and (κ,ϕ):

- *Update* α: Given $\boldsymbol{\zeta}$, a closed-form estimate of α in (70) is given by

$$\widehat{\alpha} = \left(\boldsymbol{\Upsilon}^{\mathsf{H}}(\boldsymbol{\zeta})\boldsymbol{\Upsilon}(\boldsymbol{\zeta})\right)^{-1}\boldsymbol{\Upsilon}^{\mathsf{H}}(\boldsymbol{\zeta})\boldsymbol{y}, \tag{71}$$

  where

$$\boldsymbol{\Upsilon}(\boldsymbol{\zeta}) \triangleq \left(\beta_{\min}\widetilde{\boldsymbol{\Gamma}}_1(\kappa,\phi) + \widetilde{\boldsymbol{\Gamma}}_2(\kappa,\phi)\right)^{\mathsf{T}}\boldsymbol{a}(\widehat{\boldsymbol{p}})\sqrt{E_s}. \tag{72}$$

- *Update* $\beta_{\min}$: Given α, κ, and ϕ, under the constraint of $0 \le \beta_{\min} \le 1$, the Lagrangian can be expressed as follows:

  $L(\beta_{\min},\lambda_1,\lambda_2) = \|\boldsymbol{z} - \beta_{\min}\boldsymbol{\omega}\|^2 + \lambda_1(\beta_{\min}-1) - \lambda_2\beta_{\min}$

  where $\boldsymbol{z} = \boldsymbol{y} - \alpha\widetilde{\boldsymbol{\Gamma}}_2(\kappa,\phi)^{\mathsf{T}}\boldsymbol{a}(\widehat{\boldsymbol{p}})\sqrt{E_s}$ and $\boldsymbol{\omega} = \alpha\widetilde{\boldsymbol{\Gamma}}_1(\kappa,\phi)^{\mathsf{T}}\boldsymbol{a}(\widehat{\boldsymbol{p}})\sqrt{E_s}$. From Karush-Kuhn-Tucker conditions, the closed-form estimate of $\beta_{\min}$ in (70) can be obtained from the following set of equations:

$$\lambda_1 - \lambda_2 + 2\widehat{\beta}_{\min}\boldsymbol{\omega}^{\mathsf{H}}\boldsymbol{\omega} = \boldsymbol{z}^{\mathsf{H}}\boldsymbol{\omega} + \boldsymbol{\omega}^{\mathsf{H}}\boldsymbol{z} \tag{73}$$

$$\lambda_1(\widehat{\beta}_{\min}-1) = 0, \ \ \lambda_2\widehat{\beta}_{\min} = 0. \tag{74}$$

  Hence, we can conclude that $\widehat{\beta}_{\min}$ admits one of the three alternative forms: $\widehat{\beta}_{\min} = 1$, $\widehat{\beta}_{\min} = 0$, or $\widehat{\beta}_{\min} = \mathrm{Re}\{\boldsymbol{z}^{\mathsf{H}}\boldsymbol{\omega}\}/(\boldsymbol{\omega}^{\mathsf{H}}\boldsymbol{\omega})$. Among these three solutions, the one which yields the smallest objective is chosen.
- *Update* κ *and* ϕ: Given α and $\beta_{\min}$, we can estimate κ

Algorithm 2 AML Algorithm for Joint UE Localization and Online RIS Calibration

1: **Input:** Observation $\boldsymbol{y}$ in (67), $T_{\rm thr}, J_{\max}$.
2: **Output:** Location estimate $\widehat{\boldsymbol{p}}$, channel gain estimate $\widehat{\alpha}$ and estimates of RIS amplitude model parameters $\widehat{\boldsymbol{\zeta}} = [\widehat{\beta}_{\min}, \widehat{\kappa}, \widehat{\phi}]^{\mathsf{T}}$.
3: **Step 0:** *Initialization of UE Location*
(a) Set $\beta_{\min} = 1$.
(b) Compute the initial location estimate $\widehat{\boldsymbol{p}}$ using Algorithm 1.
4: **Step 1:** *Alternating Iterations for Online RIS Calibration*
5: Set $m = 0$.
6: **while** the objective function in (70) does not converge and $m < J_{\max}$ **do**
7: Update the channel estimate $\widehat{\alpha}$ via (71).
8: Update $\widehat{\beta}_{\min}$ via (73) and (74).
9: Update $\widehat{\kappa}$ and $\widehat{\phi}$ via (75).
10: Set $m = m + 1$.
11: **end while**
12: **Step 2:** *Refinement of UE Location with Calibrated RIS Model*
(a) Use Algorithm 1 to estimate the UE location, $\widehat{\boldsymbol{p}}$, and the channel gain, $\widehat{\alpha}$, from (69) by plugging the estimates $\widehat{\beta}_{\min}$, $\widehat{\kappa}$ and $\widehat{\phi}$ obtained at the output of **Step 1**.

and ϕ via a 2-D search:

$$(\widehat{\kappa}, \widehat{\phi}) = \underset{\substack{\kappa\in[0,\kappa_{\max})\\ \phi\in[0,2\pi)}}{\arg\min} \left\| \boldsymbol{y} - \alpha \left(\beta_{\min}\widetilde{\boldsymbol{\Gamma}}_1(\kappa,\phi) + \widetilde{\boldsymbol{\Gamma}}_2(\kappa,\phi)\right)^{\mathsf{T}} \boldsymbol{a}(\widehat{\boldsymbol{p}})\sqrt{E_s} \right\| \tag{75}$$

for some finite $\kappa_{\max}$.

3) Step 2: Refinement of UE Location: As the output of this alternating procedure, we obtain the estimates of $\overline{\alpha}$, $\overline{\beta}_{\min}$, $\overline{\kappa}$, and $\overline{\phi}$. By plugging the estimates of $\overline{\beta}_{\min}$, $\overline{\kappa}$, and $\overline{\phi}$ (representing the *calibrated* RIS parameters) back into the ML estimator in (69), the estimate of the UE location $\overline{\boldsymbol{p}}$ can be refined via Algorithm 1. The overall algorithm for joint UE localization and online RIS calibration is summarized in Algorithm 2.

Remark 4. *If we skip Step 1 of Algorithm 2 (i.e., online RIS calibration) and choose $\widehat{\beta}_{\min} = 1$ (i.e., uncalibrated, unit-amplitude RIS model in* (11)*), the AML algorithm gives the same estimate as the AMML algorithm.*

C. Complexity and Convergence of Algorithm 2

We evaluate the complexity of Algorithm 2 by assuming that the search intervals for κ and ϕ are discretized into grids of size L each. If $T < T_{\rm thr}$, the overall cost of Algorithm 2 is simply equal to $\mathcal{O}\left(TM\max\{K,L\}^2\right)$, where K is defined as in Sec. IV-E. If $T \geq T_{\rm thr}$, the computational cost becomes $\mathcal{O}\left(TM\max\{K(2N+1), L^2\}\right)$. The details can be found in Appendix D.

The convergence of Algorithm 2 can be analyzed by noting that if the solutions to the subproblems of (70) via the alternating iterations in Step 1 are unique (i.e., α, $\beta_{\min}$ and (κ,ϕ) are obtained uniquely in (71), (73)-(74) and (75), respectively), then Step 1 converges to a stationary point of (70) [61, Prop. 1]. Due to the closed-form solution in (71), the uniqueness of α is guaranteed, while for $\beta_{\min}$ and (κ,ϕ) the uniqueness is satisfied with high probability via random RIS phase configurations, following the arguments in [38, Sec. IV-B].

D. Scenario-III: Known RIS Amplitude Model with Known Parameters

In this scenario, the unknown system parameters are given by $\boldsymbol{\eta} = [\mathrm{Re}(\alpha)\, \mathrm{Im}(\alpha)\, \boldsymbol{p}^{\mathsf{T}}]^{\mathsf{T}}$ and the values of the RIS related parameters are perfectly known. For this scenario, the FIM, $\boldsymbol{J}(\boldsymbol{\eta}) \in \mathbb{R}^{5\times 5}$, can be computed as in (61). In addition, the derivatives presented in Appendix E can be used by replacing $\tilde{w}_{t,m}$'s with $w_{t,m}$'s.

To estimate the UE location, we can employ the same AML algorithm, Algorithm 2, as used in Scenario-II. As the values of $\overline{\beta}_{\min}, \overline{\kappa}$, and $\overline{\phi}$ are available, we can skip Step 0 and Step 1 of Algorithm 2 and run Step 2 with the known values of the RIS amplitude model parameters.

VI. Numerical Results

In this section, we first present numerical examples for evaluating the theoretical bounds in three different scenarios, and then compare the performance of the AMML and AML estimators against the theoretical bounds.

A. Simulation Setup

We consider an RIS with $M = 50 \times 50$ elements, where the inter-element spacing is $\lambda/2$ and the area of each element is $A = \lambda^2/4$ [27]. The carrier frequency is equal to $f_c = 28$ GHz and the bandwidth is set to 1 MHz. The RIS is modeled to lie in the X-Y plane with $\boldsymbol{p}_{\rm RIS} = [0\,0\,0]^{\mathsf{T}}$. Moreover, for the RIS elements, $\theta_{t,m}$ values are generated uniformly and independently between $-\pi$ and π. In accordance with the Fresnel near-field region defined in (6), whose boundaries are 1.40 and 26.79 meters, the BS and UE are located at $\boldsymbol{p}_{\rm BS} = 5.77 \times [-1\,1\,1]^{\mathsf{T}}$ and $\overline{\boldsymbol{p}} = 2.89 \times [1\,1\,1]^{\mathsf{T}}$ meters, respectively, leading to 10 and 5 meters of distance to the RIS. We set the number of transmissions to $T = 200$, yielding a total duration of 0.2 ms. For simplicity, we assume that $s_t = \sqrt{E_s}$ for any t. Also, the SNR is defined as

$$\mathrm{SNR} = \frac{E_s\,|\overline{\alpha}|^2}{TN_0} \sum_{t=1}^{T} \left| \boldsymbol{b}^{\mathsf{T}}(\overline{\boldsymbol{p}})\boldsymbol{w}_t \right|^2 . \tag{76}$$

To solve (24) for the LB computation, we employ the GlobalSearch algorithm of MATLAB by providing $\overline{\boldsymbol{p}}$ as the initial vector. For the Jacobi-Anger approximation in (48), $\frac{2\pi}{\lambda} q_{\max} \sin\vartheta$ in (49) evaluates to 90.7 for the considered setup, while we set $N = 50$, which turns out to be sufficient for the proposed algorithms to converge to their respective theoretical bounds. Furthermore, we set $T_{\rm thr} = 2N + 1$, $\kappa_{\max} = 5$ and $I_{\max} = J_{\max} = 5$ in Algorithm 1 and Algorithm 2. Since $T \geq T_{\rm thr}$, Algorithm 1 chooses the Jacobi-Anger based branch. To evaluate the performance of the branch $T < T_{\rm thr}$, we also show simulation results for $T = 10$.

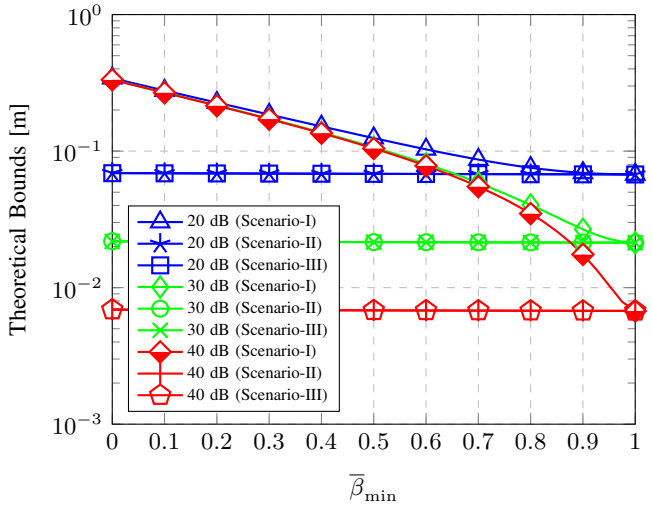

Fig. 3. Theoretical bounds versus $\overline{\beta}_{\min}$ for SNR = 20 dB, 30 dB and 40 dB when the UE distance is 5 meters, $\overline{\kappa} = 1.5$ and $\overline{\phi} = 0$.

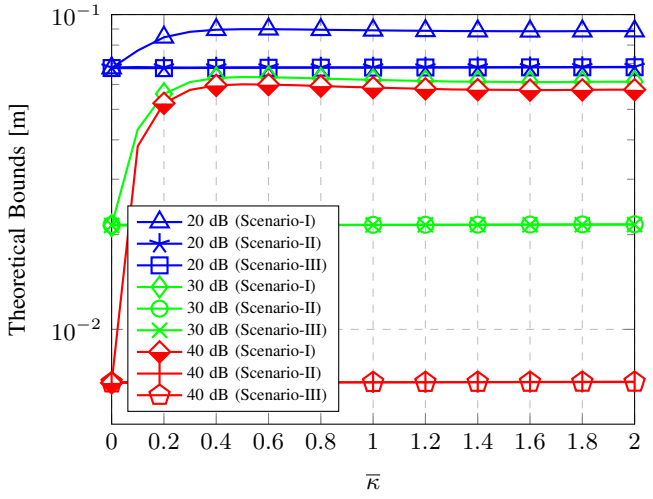

Fig. 4. Theoretical bounds versus $\overline{\kappa}$ for SNR = 20 dB, 30 dB and 40 dB when the UE distance is 5 meters, $\overline{\beta}_{\min} = 0.7$ and $\overline{\phi} = 0$.

B. Results and Discussions

1) Theoretical Limits vs. RIS Model Parameters: In Fig. 3, for all the three scenarios, we show the theoretical bounds as a function of $\overline{\beta}_{\min}$ for SNRs of 20, 30, and 40 dB when the UE distance is 5 meters from the center of the RIS, $\overline{\kappa} = 1.5$, and $\overline{\phi} = 0$. We observe from the figure that as $\overline{\beta}_{\min}$ decreases, i.e., as the mismatch between the true and the assumed models increases, the LB increases and raising the SNR level does not improve the LB values significantly. In addition, the sensitivity to the model mismatch is more pronounced at higher SNRs, while for an SNR of 20 dB, the performance is relatively insensitive for $\overline{\beta}_{\min} > 0.7$. This shows that being unaware of the true RIS amplitude model can constitute a crucial limiting factor for RIS-aided localization at high SNRs. Interestingly, we note that when the true model and the true values of $\overline{\beta}_{\min}$, $\overline{\kappa}$ and $\overline{\phi}$ are known, the value of $\overline{\beta}_{\min}$ does not influence the CRB values notably. In fact, as the CRB values for the Scenario-II and Scenario-III are almost the same, it can be inferred that once we know the true model, knowing the true values of $\overline{\beta}_{\min}$, $\overline{\kappa}$ and $\overline{\phi}$ is not critical.

In Fig. 4, for all the three scenarios, the theoretical bounds are plotted versus κ for SNRs of 20, 30, and 40 dB when the UE distance is 5 meters from the center of the RIS, $\overline{\beta}_{\min} = 0.7$, and $\overline{\phi} = 0$. Similar to Fig. 3, the CRB values for Scenario-II and Scenario-III are almost the same. We also observe that as κ approaches 0, i.e., as the mismatch between the true and assumed models decreases, the LB and the CRB values for Scenario-II and Scenario-III become closer to each other similarly to Fig. 3. In addition, as the SNR increases, the performance loss due to the mismatch becomes more significant. Moreover, increasing $\overline{\kappa}$ beyond $\overline{\kappa} = 0.4$ does not have any notable impacts on the LB values.

2) Effect of RIS Size: To investigate the effects of the number of RIS elements, the average LB and CRB values are plotted versus the RIS size in Fig. 5 for all the three scenarios by averaging over 200 different random phase profiles for the RIS elements, where the SNR is 20 dB, the UE distance is 5 meters, $\overline{\beta}_{\min} \in \{0.3, 0.7\}$, $\overline{\kappa} = 1.5$, and $\overline{\phi} = 0$. We observe that as the RIS size or $\overline{\beta}_{\min}$ increases, we obtain

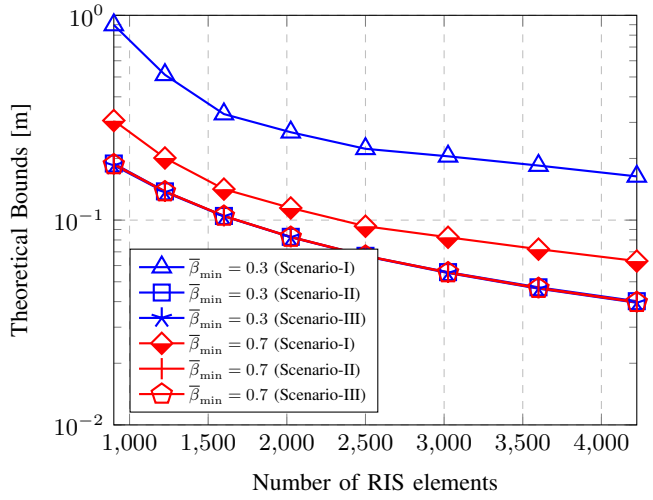

Fig. 5. Theoretical bounds versus number of RIS elements and for $\overline{\beta}_{\min} \in \{0.3, 0.7\}$ when the UE distance is 5 meters, SNR = 20 dB, $\overline{\kappa} = 1.5$ and $\overline{\phi} = 0$.

lower LB values in general. In addition, the curves for different $\overline{\beta}_{\min}$ values are almost parallel. We also note the significant price paid due to the model mismatch: With the perfect knowledge of the RIS model and with 1000 elements, a similar performance can only be attained using a RIS with 4225 elements when $\overline{\beta}_{\min} = 0.3$ under the model mismatch.

3) Performance of Algorithm 1 and Algorithm 2 vs. SNR: To provide a comparative analysis of the three scenarios, in Fig. 6, the performances of the AMML algorithm in Algorithm 1 and the AML algorithm in Algorithm 2 are plotted versus SNR, and compared with the corresponding LB and CRB values when $\overline{\beta}_{\min} = 0.5$. It is noted that the AMML and AML algorithms achieve the theoretical bounds in the high SNR regime in all the three scenarios. This indicates that the proposed Jacobi-Anger expansion based low-complexity approach in Algorithm 1 can successfully provide near-optimal solutions to the near-field localization problem in (34). Moreover, by comparing the AMML and the AML curves at high SNRs, we observe that the AML

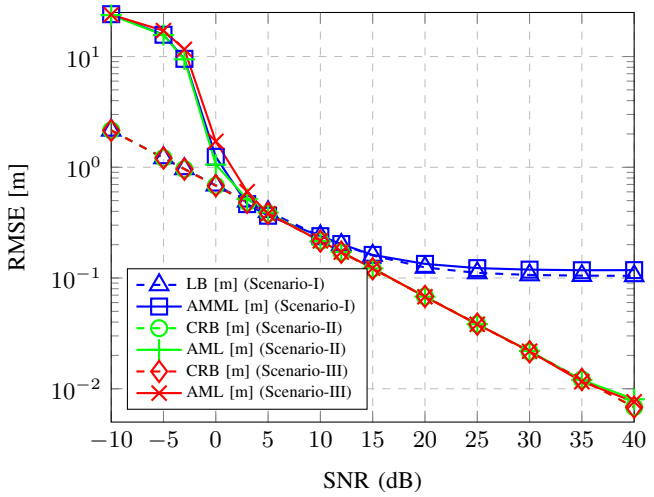

Fig. 6. Performance of the AMML and the AML algorithms along with the corresponding theoretical bounds versus SNR (dB) when the UE distance is 5 meters, $\overline{\kappa} = 1.5$, $\overline{\beta}_{\min} = 0.5$ and $\overline{\phi} = 0$.

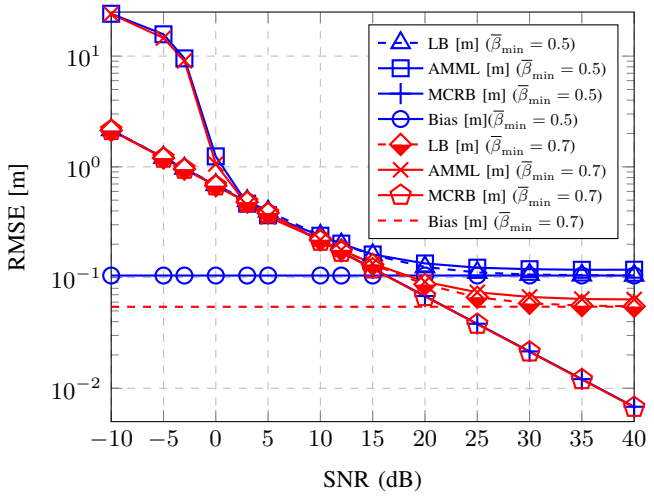

Fig. 7. AMML, LB, MCRB, and Bias term versus SNR (dB) for $\overline{\beta}_{\min} \in \{0.5, 0.7\}$ when the UE distance is 5 meters, $\overline{\kappa} = 1.5$ and $\overline{\phi} = 0$.

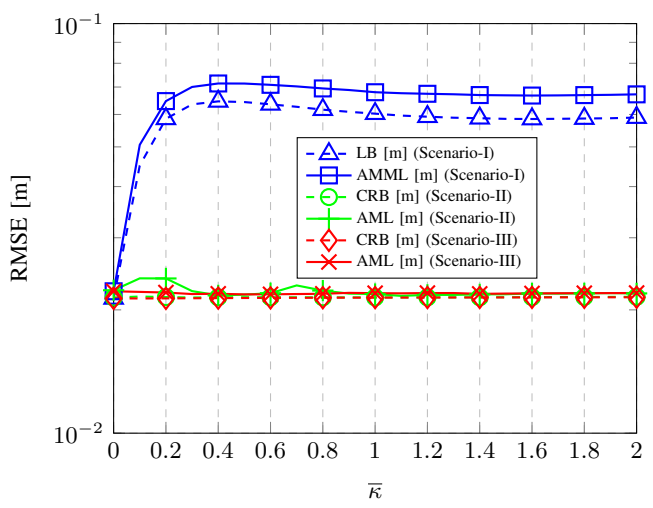

Fig. 8. Performance of the AMML and the AML algorithms along with the corresponding theoretical bounds versus $\overline{\kappa}$ when the UE distance is 5 meters, SNR = 30 dB, $\overline{\beta}_{\min} = 0.7$, and $\overline{\phi} = 0$.

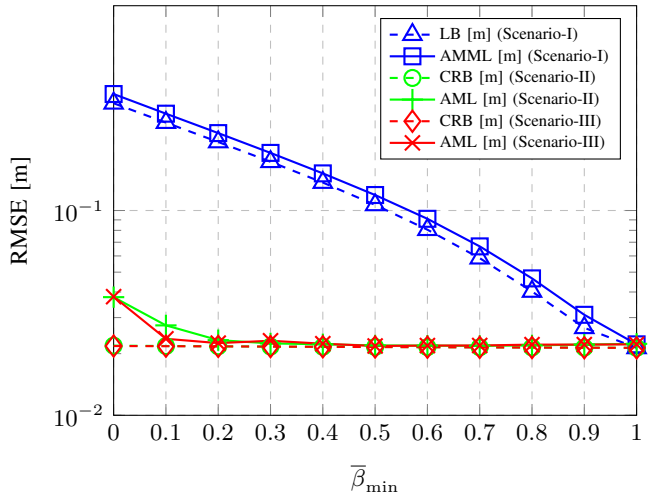

Fig. 9. Performance of the AMML and the AML algorithms along with the corresponding theoretical bounds versus $\overline{\beta}_{\min}$ when the UE distance is 5 meters, SNR = 30 dB, $\overline{\kappa} = 1.5$, and $\overline{\phi} = 0$.

algorithm completely recovers the performance loss due to model misspecification, which verifies the effectiveness of the online RIS calibration in Step 1 and the UE location refinement in Step 2 of Algorithm 2.

To explore the asymptotic behavior of the AMML algorithm in Scenario I, its performance with respect to SNR is illustrated in Fig. 7 for $\overline{\beta}_{\min} = 0.5$ and 0.7 when the UE distance is 5 meters. In addition to the performance of the AMML estimator, the LB, the MCRB, and the bias term values are also plotted. We observe that the AMML estimator exhibits three distinct regimes: a low-SNR regime where the AMML is limited by noise peaks and thus far away from the LB; a medium-SNR regime where the AMML is close to the LB, which itself is dominated by the MCRB; and a high-SNR regime, where the AMML and LB are limited by the bias term $(\boldsymbol{\eta}_0)$.

4) Performance of Algorithm 1 and Algorithm 2 vs. RIS Model Parameters: To investigate the performance of the proposed localization methods under varying values of RIS model parameters, in Fig. 8, the RMSEs of the AMML and AML algorithms are evaluated versus $\overline{\kappa}$ when SNR = 30 dB, $\overline{\beta}_{\min} = 0.7$, $\overline{\phi} = 0$, and the UE distance is 5 meters. Similarly, in Fig. 9, the performances of the AMML and AML algorithms versus $\overline{\beta}_{\min}$ are shown when SNR = 30 dB, $\overline{\kappa} = 1.5$, $\overline{\phi} = 0$, and the UE distance is 5 meters. From Figs. 8 and 9, it is noted that for Scenario-II and Scenario-III, the AML algorithm achieves the CRB, which is insensitive to the values of $\overline{\kappa}$ and $\overline{\beta}_{\min}$. In addition, a combined evaluation of Fig. 6, Fig. 8 and Fig. 9 demonstrates that both of the proposed algorithms can attain the corresponding bounds under a wide variety of settings concerning different SNR levels and RIS model parameters.

5) Convergence Behavior of Algorithm 2: Finally, for a single realization, Fig. 10 illustrates the errors of the position estimates at each alternating iteration in Step 1 of Algorithm 2. In the figure, $\hat{\boldsymbol{p}}(k)$ denotes the estimate of the position $\overline{\boldsymbol{p}}$ obtained from the Jacobi-Anger approach by using the

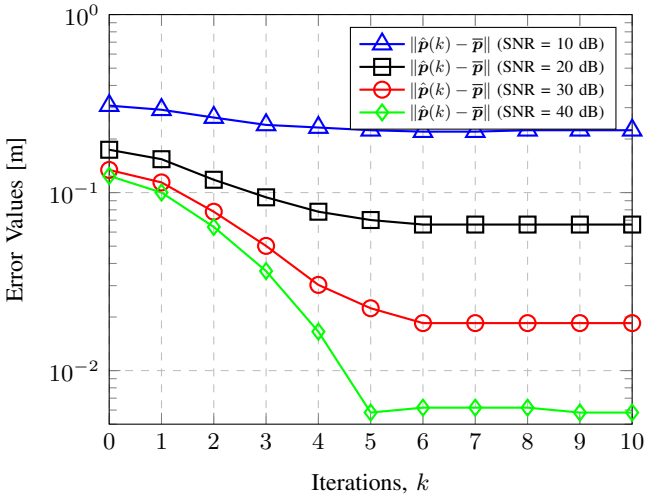

Fig. 10. Errors of estimates of $\overline{\boldsymbol{p}}$ at each iteration in Step 1 of Algorithm 2 when $\overline{\beta}_{\min}=0.5$, $\overline{\kappa}=1.5$, $\overline{\phi}=0$, and UE distance is 5 meters.

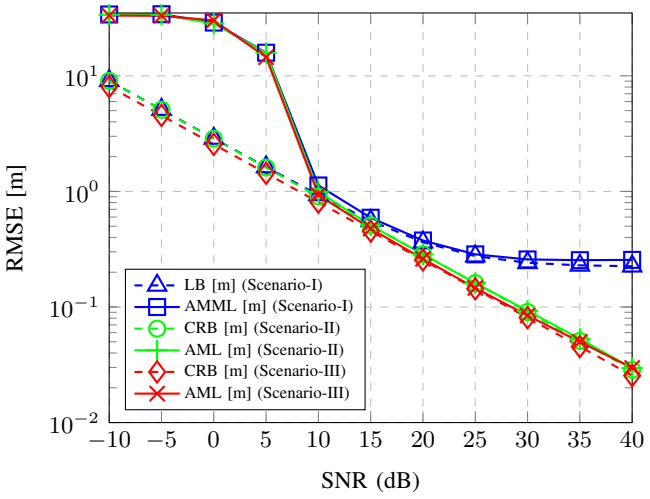

Fig. 11. Performance of the AMML and the AML algorithms along with the corresponding theoretical bounds versus SNR (dB) when the UE distance is 5 meters, $\overline{\kappa}=1.5$, $\overline{\beta}_{\min}=0.7$, $\overline{\phi}=0$, and $T=10$.

estimate of $\overline{\boldsymbol{\zeta}}$ at the k-th iteration.

We observe that, starting from the initial location estimate given by Algorithm 1, Algorithm 2 provides significant performance gains through the iterations of the online RIS calibration in Step 1. In particular, at an SNR of 40 dB, Algorithm 2 achieves the error value of $0.0058\,\mathrm{m}$, while the error corresponding to Algorithm 1 is $0.1241\,\mathrm{m}$.

6) Numerical Results for Small Number of Observations: In this part, we use the same simulation setup described in Sec. VI-A by only changing T from 200 to 10. In Fig. 11, performances of the AMML and AML algorithms versus SNR are presented when $\overline{\beta}_{\min}=0.7$, $\overline{\kappa}=1.5$, $\overline{\phi}=0$. It can be observed that when the number of transmissions is reduced to 10, the proposed algorithms are still capable of achieving the theoretical performance bounds in all three scenarios.

VII. Concluding Remarks

We have studied the problem of RIS-aided near-field localization under amplitude variations of individual RIS elements as a function of the applied phase shifts, which is a practical model based on equivalent RIS circuit models of reflecting elements [35]. First, through the MCRB analysis, we have quantified localization performance losses due to model misspecification when the UE is unaware of the RIS amplitude model, and developed an algorithm that achieves the corresponding LB. Second, under a known RIS amplitude model, we have derived the corresponding CRB and proposed a low-complexity algorithm for joint UE localization and online calibration of RIS model parameters. Extensive simulations over a broad range of operating conditions demonstrate the following key results:

- *Significance of the Knowledge of RIS Amplitude Model:* Being unaware of the true RIS amplitude model and assuming conventional unit-amplitude RIS responses can severely degrade the localization accuracy, with the losses being more pronounced at higher SNRs and higher amplitude fluctuations (small $\overline{\beta}_{\min}$ and large $\overline{\kappa}$ in (8)).
- *Localization under Model Mismatch:* Under the unknown RIS amplitude model, the proposed Jacobi-Anger expansion based low-complexity method in Algorithm 1 can provide near-optimal localization performance very close to the corresponding LB.
- *Joint Localization and RIS Calibration:* Under the known RIS amplitude model, it is possible to recover the performance losses incurred by model misspecification using the proposed algorithm in Algorithm 2, which can calibrate the RIS model online with the aid of an unknown-location UE and subsequently refine the UE location with an accuracy that asymptotically attains the CRB.

Based on these outcomes, future research will focus on localization-optimal passive beamforming at the RIS under the realistic RIS amplitude model in (8), considering wideband signals, unobstructed LoS scenarios and the effect of MC between RIS elements. In addition, data-driven approaches will be considered to learn the mapping from RIS phases to amplitudes in the absence of a specific functional form as in (8), which would enable generalizing the proposed approach to any type of RIS.

Appendix A
Proof of Lemma 1

Based on the definition of the KL divergence and the system model in Section II, (14) can be expressed as

$$\boldsymbol{\eta}_0 = \underset{\boldsymbol{\eta}\in\mathbb{R}^5}{\arg\min} \int p(\boldsymbol{y}) \log\left(\frac{p(\boldsymbol{y})}{\tilde{p}(\boldsymbol{y}|\boldsymbol{\eta})}\right) \mathrm{d}\boldsymbol{y} \tag{77}$$

$$= \underset{\boldsymbol{\eta}\in\mathbb{R}^5}{\arg\min} - \int p(\boldsymbol{y}) \log \tilde{p}(\boldsymbol{y}|\boldsymbol{\eta}) \,\mathrm{d}\boldsymbol{y} \tag{78}$$

$$= \underset{\boldsymbol{\eta}\in\mathbb{R}^5}{\arg\min} \int p(\boldsymbol{y}) \left\|\boldsymbol{y}-\tilde{\boldsymbol{\mu}}(\boldsymbol{\eta})\right\|^2 \mathrm{d}\boldsymbol{y} \tag{79}$$

where the second equality is due to the independence of $p(\boldsymbol{y})$ from $\boldsymbol{\eta}$, and the last equality is obtained from (12). Then, it can be shown that the following equations hold:

$$\int p(\boldsymbol{y}) \left\|\boldsymbol{y}-\tilde{\boldsymbol{\mu}}(\boldsymbol{\eta})\right\|^2 d\boldsymbol{y} = \sum_{t=1}^{T} \int p(\boldsymbol{y}) \left|y_t-\tilde{\mu}_t(\boldsymbol{\eta})\right|^2 \mathrm{d}\boldsymbol{y}$$

$$= \sum_{t=1}^{T} \underbrace{\left(\prod_{t' \neq t} \int p(y_{t'}) \, \mathrm{d}y_{t'} \right)}_{=1} \left(\int p(y_t) \left| y_t - \tilde{\mu}_t(\boldsymbol{\eta}) \right|^2 \mathrm{d}y_t \right)$$

$$= \sum_{t=1}^{T} \int p(y_t) \left| y_t - \tilde{\mu}_t(\boldsymbol{\eta}) \right|^2 \mathrm{d}y_t. \tag{80}$$

We now introduce $\epsilon_t(\boldsymbol{\eta}) = \mu_t - \tilde{\mu}_t(\boldsymbol{\eta})$, so that $\left| y_t - \tilde{\mu}_t(\boldsymbol{\eta}) \right|^2 = \left| y_t - \mu_t + \epsilon_t(\boldsymbol{\eta}) \right|^2$, and the integral expression in (80) can be manipulated as follows:

$$\int p(y_t) \left| y_t - \tilde{\mu}_t(\boldsymbol{\eta}) \right|^2 \mathrm{d}y_t = \int p(y_t) \left| y_t - \mu_t \right|^2 \mathrm{d}y_t + \left| \epsilon_t(\boldsymbol{\eta}) \right|^2 \int p(y_t) \, \mathrm{d}y_t + 2 \int p(y_t) \mathrm{Re}\left((y_t - \mu_t)^* \epsilon_t(\boldsymbol{\eta}) \right) \mathrm{d}y_t. \tag{81}$$

Since $y_t \sim \mathcal{CN}(\mu_t, N_0)$ and $\int p(y_t) \, \mathrm{d}y_t = 1$, the expression in (81) can be simplified as

$$\int p(y_t) \left| y_t - \tilde{\mu}_t(\boldsymbol{\eta}) \right|^2 \mathrm{d}y_t = N_0 + \left| \epsilon_t(\boldsymbol{\eta}) \right|^2. \tag{82}$$

By combining (79), (80) and (82), we finally obtain that

$$\bar{\boldsymbol{\eta}} = \underset{\boldsymbol{\eta} \in \mathbb{R}^5}{\arg\min} \sum_{t=1}^{T} \left(N_0 + \left| \epsilon_t(\boldsymbol{\eta}) \right|^2 \right) = \underset{\boldsymbol{\eta} \in \mathbb{R}^5}{\arg\min} \sum_{t=1}^{T} \left| \epsilon_t(\boldsymbol{\eta}) \right|^2,$$

which completes the proof.

Appendix B
Proof of Lemma 2

Let $\boldsymbol{\mu}^{(k)} = \{\mu_t^{(k)}\}_{t=1}^{T^{(k)}}$ and $\tilde{\boldsymbol{\mu}}^{(k)}(\boldsymbol{\eta}) = \{\tilde{\mu}_t^{(k)}(\boldsymbol{\eta})\}_{t=1}^{T^{(k)}}$ be the set of the noiseless transmitted signals for the k-th set of observations under the true model and assumed model, respectively for a given parameter $\boldsymbol{\eta}$. (32) implies that $\mu_t^{(2)} = \mu_{\left(t \bmod T^{(1)}\right)}^{(1)}$ for any $1 \leq t \leq T^{(2)}$. Hence, it can be stated that

$$\left\| \boldsymbol{\mu}^{(2)} - \tilde{\boldsymbol{\mu}}^{(2)}(\boldsymbol{\eta}) \right\|^2 = \sum_{t=1}^{T^{(2)}} \left| \mu_t^{(2)} - \tilde{\mu}_t^{(2)}(\boldsymbol{\eta}) \right|^2, \tag{83}$$

$$= K \left\| \boldsymbol{\mu}^{(1)} - \tilde{\boldsymbol{\mu}}^{(1)}(\boldsymbol{\eta}) \right\|^2, \tag{84}$$

which implies $\boldsymbol{\eta}_0^{(1)} = \boldsymbol{\eta}_0^{(2)}$. This means that the Bias term in (20) remains the same even though the number of transmissions is increased from $T^{(1)}$ to $T^{(2)}$. That is, if $\mathrm{Bias}\big(T^{(k)}, \boldsymbol{\eta}_0^{(k)}\big)$ denotes the corresponding Bias for the k-th set of observations, we have $\mathrm{Bias}\big(T^{(1)}, \boldsymbol{\eta}_0^{(1)}\big) = \mathrm{Bias}\big(T^{(2)}, \boldsymbol{\eta}_0^{(2)}\big)$.

Now, let us compare the MCRB expressions for both cases. To stress the dependence on the number of observations, we will replace $\boldsymbol{A}_{\boldsymbol{\eta}_0}$ and $\boldsymbol{B}_{\boldsymbol{\eta}_0}$ in (17) and (18) with $\boldsymbol{A}_{T,\boldsymbol{\eta}_0}$ and $\boldsymbol{B}_{T,\boldsymbol{\eta}_0}$ when the number of transmissions is equal to T. By using (29), for any i, j, it can be seen that

$$[\boldsymbol{A}_{T^{(2)},\boldsymbol{\eta}_0^{(2)}}]_{i,j} = K [\boldsymbol{A}_{T^{(1)},\boldsymbol{\eta}_0^{(1)}}]_{i,j}. \tag{85}$$

For $k \in \{1, 2\}$ and any i, j, we define $\boldsymbol{R}_{T^{(k)},\boldsymbol{\eta}_0^{(k)}}$ and $\boldsymbol{S}_{T^{(k)},\boldsymbol{\eta}_0^{(k)}}$ as follows:

$$[\boldsymbol{R}_{T^{(k)},\boldsymbol{\eta}_0^{(k)}}]_{i,j} \triangleq \frac{4}{N_0^2} \left[\mathrm{Re}\left\{ \boldsymbol{\epsilon}^{(k)}(\boldsymbol{\eta})^{\mathsf{H}} \frac{\partial \tilde{\boldsymbol{\mu}}^{(k)}(\boldsymbol{\eta})}{\partial \eta_i} \right\} \mathrm{Re}\left\{ \boldsymbol{\epsilon}^{(k)}(\boldsymbol{\eta})^{\mathsf{H}} \frac{\partial \tilde{\boldsymbol{\mu}}^{(k)}(\boldsymbol{\eta})}{\partial \eta_j} \right\} \right] \Bigg|_{\boldsymbol{\eta} = \boldsymbol{\eta}_0^{(k)}}, \tag{86}$$

$$[\boldsymbol{S}_{T^{(k)},\boldsymbol{\eta}_0^{(k)}}]_{i,j} \triangleq \frac{2}{N_0} \left[\mathrm{Re}\left\{ \left(\frac{\partial \tilde{\boldsymbol{\mu}}^{(k)}(\boldsymbol{\eta})}{\partial \eta_i} \right)^{\mathsf{H}} \frac{\partial \tilde{\boldsymbol{\mu}}^{(k)}(\boldsymbol{\eta})}{\partial \eta_j} \right\} \right] \Bigg|_{\boldsymbol{\eta} = \boldsymbol{\eta}_0^{(k)}}. \tag{87}$$

It can easily be verified that both $\boldsymbol{R}_{T^{(k)},\boldsymbol{\eta}_0^{(k)}}$ and $\boldsymbol{S}_{T^{(k)},\boldsymbol{\eta}_0^{(k)}}$ are positive-definite matrices for any $k \in \{1, 2\}$. Based on (86) and (87), we can write

$$[\boldsymbol{B}_{T^{(2)},\boldsymbol{\eta}_0^{(2)}}] = [\boldsymbol{R}_{T^{(2)},\boldsymbol{\eta}_0^{(2)}}] + [\boldsymbol{S}_{T^{(2)},\boldsymbol{\eta}_0^{(2)}}] = K^2 [\boldsymbol{R}_{T^{(1)},\boldsymbol{\eta}_0^{(1)}}] + K [\boldsymbol{S}_{T^{(1)},\boldsymbol{\eta}_0^{(1)}}] \tag{88}$$

By using (85) and (88), it is possible to express $\mathrm{MCRB}\big(T^{(2)}, \boldsymbol{\eta}_0^{(2)}\big)$ as follows:

$$\mathrm{MCRB}\big(T^{(2)}, \boldsymbol{\eta}_0^{(2)}\big) = \frac{1}{K^2} \big(\boldsymbol{A}_{T^{(1)},\boldsymbol{\eta}_0^{(1)}}\big)^{-1} \tag{89}$$

$$\times \left(K^2 [\boldsymbol{R}_{T^{(1)},\boldsymbol{\eta}_0^{(1)}}] + K [\boldsymbol{S}_{T^{(1)},\boldsymbol{\eta}_0^{(1)}}] \right) \big(\boldsymbol{A}_{T^{(1)},\boldsymbol{\eta}_0^{(1)}}\big)^{-1}. \tag{90}$$

Since $\boldsymbol{R}_{T^{(1)},\boldsymbol{\eta}_0^{(1)}}$, $\boldsymbol{S}_{T^{(1)},\boldsymbol{\eta}_0^{(1)}}$ and $\boldsymbol{A}_{T^{(1)},\boldsymbol{\eta}_0^{(1)}}$ are positive-definite matrices, $\mathrm{Tr}\left\{ \left([\boldsymbol{R}_{T^{(1)},\boldsymbol{\eta}_0^{(1)}}] \right) \big(\boldsymbol{A}_{T^{(1)},\boldsymbol{\eta}_0^{(1)}}\big)^{-2} \right\} \geq 0$ and $\mathrm{Tr}\left\{ \left([\boldsymbol{S}_{T^{(1)},\boldsymbol{\eta}_0^{(1)}}] \right) \big(\boldsymbol{A}_{T^{(1)},\boldsymbol{\eta}_0^{(1)}}\big)^{-2} \right\} \geq 0$. This implies that for $K \geq 2$,

$$\frac{1}{K} < \frac{\mathrm{Tr}\left\{ \mathrm{MCRB}\big(T^{(2)}, \boldsymbol{\eta}_0^{(2)}\big) \right\}}{\mathrm{Tr}\left\{ \mathrm{MCRB}\big(T^{(1)}, \boldsymbol{\eta}_0^{(1)}\big) \right\}} < 1. \tag{91}$$

Furthermore, since $\mathrm{Bias}\big(T^{(1)}, \boldsymbol{\eta}_0^{(1)}\big) = \mathrm{Bias}\big(T^{(2)}, \boldsymbol{\eta}_0^{(2)}\big)$, the latter conclusion for the ratio of the trace of the LBs, is evident from (91). For the CRB calculation, as stated in Remark 3, when there is no mismatch between the assumed model and the true model, we can write

$$\mathrm{CRB}\big(T^{(k)}\big) = \big(\boldsymbol{A}_{T^{(k)},\overline{\boldsymbol{\eta}}}\big)^{-1} \tag{92}$$

for $k \in \{1, 2\}$. It is evident from (85) and (92) that

$$\frac{\mathrm{Tr}\left\{ \mathrm{CRB}\big(T^{(2)}\big) \right\}}{\mathrm{Tr}\left\{ \mathrm{CRB}\big(T^{(1)}\big) \right\}} = \frac{\mathrm{Tr}\left\{ \big(\boldsymbol{A}_{T^{(2)},\overline{\boldsymbol{\eta}}}\big)^{-1} \right\}}{\mathrm{Tr}\left\{ \big(\boldsymbol{A}_{T^{(1)},\overline{\boldsymbol{\eta}}}\big)^{-1} \right\}} = \frac{1}{K} \tag{93}$$

as we desired to prove.

Appendix C
Computational Complexity of Algorithm 1

First assume that $T < T_{\mathrm{thr}}$. It is clear that complexity of Algorithm 1 is dominated by the 2-D search for estimating azimuth and elevation angles. In the algorithm we equate $I_{\max}$ to 5. That is, for Algorithm 1, it is sufficient to analyze the computational complexity of the 2-D search given in (39). Let us define $\boldsymbol{x}(\vartheta, \varphi) \triangleq \boldsymbol{Q}\boldsymbol{a}(\vartheta, \varphi)\sqrt{E_s}$. The computational cost of $\boldsymbol{x}(\vartheta, \varphi)$ is simply equal to $\mathcal{O}(TM)$. One should note that, (39) is equivalent to the following problem

$$(\widehat{\vartheta},\widehat{\varphi}) = \arg\max_{\vartheta,\varphi} \frac{\boldsymbol{x}(\vartheta,\varphi)^{\mathsf{H}}\boldsymbol{y}}{\|\boldsymbol{x}(\vartheta,\varphi)\|^2}\ . \tag{94}$$

Hence after computing $\boldsymbol{x}(\vartheta,\varphi)$, we need to search over ϑ and φ. Therefore, the overall cost of Algorithm 1 for $T \leq T_{\rm thr}$ is $\mathcal{O}(TK^2M)$.

When $T \geq T_{\rm thr}$, the complexity of Algorithm 1 is dominated by the estimation of ϑ. To estimate ϑ, we need to compute $\boldsymbol{X}(\vartheta) \triangleq \boldsymbol{Q}\boldsymbol{G}^{\mathsf{T}}(\vartheta)$ first. The computational cost of $\boldsymbol{X}(\vartheta)$ is $\mathcal{O}\left(TM(2N+1)\right)$. Then, we need to compute the pseudo-inverse of $\boldsymbol{X}(\vartheta)$, whose computational cost is given by $\mathcal{O}\left(T(2N+1)^2\right)$ since $T \geq 2N+1$. After computing the pseudo-inverse of $\boldsymbol{X}(\vartheta)$, we need to search ϑ over $[0,\pi/2]$ to find the minimum of $\left\|\boldsymbol{y} - \boldsymbol{X}(\vartheta)\boldsymbol{X}^{\dagger}(\vartheta)\boldsymbol{y}\right\|$. That is, the overall cost of Algorithm 1 when $T \geq T_{\rm thr}$ is given by $\mathcal{O}\left(T^2(2N+1)K\right) + \mathcal{O}\left(TM(2N+1)K\right) = \mathcal{O}\left(TK(2N+1)\max\{T,M\}\right) = \mathcal{O}\left(TM(2N+1)K\right)$.

Appendix D
Computational Complexity of Algorithm 2

Similar to Algorithm 1, the computational complexity of Algorithm 2 is dominated by the 2-D search for κ and ϕ. We need to compute $\left\|\boldsymbol{y} - \alpha\left(\beta_{\min}\widetilde{\boldsymbol{\Gamma}}_1(\kappa,\phi) + \widetilde{\boldsymbol{\Gamma}}_2(\kappa,\phi)\right)^{\mathsf{T}}\boldsymbol{a}(\widehat{\boldsymbol{p}})\sqrt{E_s}\right\|$, whose computational cost is $\mathcal{O}(TM)$, for a given $\boldsymbol{\zeta}$ and α. Since we search over κ and ϕ's, the total computational complexity becomes $\mathcal{O}(TML^2)$.

Appendix E
Derivation of Entries in the MCRB

Let $\boldsymbol{\eta}$ be given by $\boldsymbol{\eta} = [\alpha_r\,\alpha_i\,\mathrm{x}\,\mathrm{y}\,\mathrm{z}]^{\mathsf{T}}$. Also, define $\boldsymbol{p} \triangleq [\mathrm{x}\,\mathrm{y}\,\mathrm{z}]^{\mathsf{T}}$, $b_m \triangleq [\boldsymbol{b}(\boldsymbol{p})]_m$, and $\alpha \triangleq \alpha_r + j\alpha_i$. We also introduce $\boldsymbol{u} = \frac{\boldsymbol{p}-\boldsymbol{p}_{\rm RIS}}{\|\boldsymbol{p}-\boldsymbol{p}_{\rm RIS}\|}$ and for any $1 \leq m \leq M$, $\boldsymbol{u}_m = \frac{\boldsymbol{p}-\boldsymbol{p}_m}{\|\boldsymbol{p}-\boldsymbol{p}_m\|}$, where $\boldsymbol{u} = [u_x\,u_y\,u_z]^{\mathsf{T}}$ and $\boldsymbol{u}_m = [u_{m,x}\,u_{m,y}\,u_{m,z}]^{\mathsf{T}}$.Then, the first and second derivatives of $\tilde{\mu}_t(\boldsymbol{\eta})$ with respect to $\boldsymbol{\eta}$ are given as follows:

$$\frac{\partial\tilde{\mu}_t(\boldsymbol{\eta})}{\partial\alpha_r} = \sum_{m=1}^{M} b_m\tilde{w}_{t,m}s_t,\ \frac{\partial\tilde{\mu}_t(\boldsymbol{\eta})}{\partial\alpha_i} = j\sum_{m=1}^{M} b_m\tilde{w}_{t,m}s_t.$$

For $\nu \in \{\mathrm{x}\,\mathrm{y}\,\mathrm{z}\}$, we can write

$$\frac{\partial\tilde{\mu}_t(\boldsymbol{\eta})}{\partial\nu} = -j\frac{2\pi}{\lambda}\alpha\sum_{m=1}^{M} b_m\left(u_{m,\nu} - u_x\right)\tilde{w}_{t,m}s_t,$$

$$\frac{\partial^2\tilde{\mu}_t(\boldsymbol{\eta})}{\partial\alpha_r\partial\nu} = -j\frac{2\pi}{\lambda}\sum_{m=1}^{M} b_m\left(u_{m,\nu} - u_\nu\right)\tilde{w}_{t,m}s_t,$$

$$\frac{\partial^2\tilde{\mu}_t(\boldsymbol{\eta})}{\partial\alpha_i\partial\nu} = j\frac{\partial^2\tilde{\mu}_t(\boldsymbol{\eta})}{\partial\alpha_r\partial\nu},$$

$$\frac{\partial^2\tilde{\mu}_t(\boldsymbol{\eta})}{\partial\nu\partial\nu} = -\alpha\frac{4\pi^2}{\lambda^2}\sum_{m=1}^{M} b_m\left(u_{m,\nu} - u_\nu\right)^2\tilde{w}_{t,m}s_t$$
$$- j\frac{2\pi}{\lambda}\alpha\sum_{m=1}^{M} b_m\left(\frac{1-u_{m,\nu}^2}{\|\boldsymbol{p}-\boldsymbol{p}_m\|} - \frac{1-u_\nu^2}{\|\boldsymbol{p}-\boldsymbol{p}_{\rm RIS}\|}\right)\tilde{w}_{t,m}s_t.$$

Moreover, if $\nu_1,\nu_2 \in \{\mathrm{x}\,\mathrm{y}\,\mathrm{z}\}$ and they correspond to different coordinates, it is possible to express

$$\frac{\partial^2\tilde{\mu}_t(\boldsymbol{\eta})}{\partial\nu_1\partial\nu_2} = -\alpha\frac{4\pi^2}{\lambda^2}\sum_{m=1}^{M} b_m\left(u_{m,\nu_1} - u_{\nu_1}\right)\left(u_{m,\nu_2} - u_{\nu_2}\right)\tilde{w}_{t,m}s_t$$
$$+ j\frac{2\pi}{\lambda}\alpha\sum_{m=1}^{M} b_m\left(\frac{u_{m,\nu_1}u_{m,\nu_2}}{\|\boldsymbol{p}-\boldsymbol{p}_m\|} - \frac{u_{\nu_1}u_{\nu_2}}{\|\boldsymbol{p}-\boldsymbol{p}_{\rm RIS}\|}\right)\tilde{w}_{t,m}s_t.$$

Appendix F
Derivatives for FIM Computation in (61)

The derivatives of μ_t with respect to the RIS model parameters $\beta_{\min}$, κ and ϕ, used for FIM computation in (61), are given by

$$\frac{\partial\mu_t(\boldsymbol{\eta})}{\partial\beta_{\min}} = \alpha\sqrt{E_s}\sum_{m=1}^{M}[\boldsymbol{b}(\boldsymbol{p})]_m e^{j\theta_{t,m}} \times\left(1 - \left(\frac{\sin(\theta_{t,m}-\phi)+1}{2}\right)^{\kappa}\right),$$

$$\frac{\partial\mu_t(\boldsymbol{\eta})}{\partial\kappa} = \alpha\sqrt{E_s}\sum_{m=1}^{M}[\boldsymbol{b}(\boldsymbol{p})]_m e^{j\theta_{t,m}}(1-\beta_{\min}) \times\left(\frac{\sin(\theta_{t,m}-\phi)+1}{2}\right)^{\kappa}\log\left(\frac{\sin(\theta_{t,m}-\phi)+1}{2}\right),$$

$$\frac{\partial\mu_t(\boldsymbol{\eta})}{\partial\phi} = -\alpha\sqrt{E_s}\sum_{m=1}^{M}[\boldsymbol{b}(\boldsymbol{p})]_m e^{j\theta_{t,m}}(1-\beta_{\min}) \times\kappa\left(\frac{\sin(\theta_{t,m}-\phi)+1}{2}\right)^{\kappa-1}\left(\frac{\cos(\theta_{t,m}-\phi)}{2}\right).$$

References

[1] W. Saad *et al.*, "A vision of 6G wireless systems: Applications, trends, technologies, and open research problems," *IEEE Netw.*, vol. 34, no. 3, pp. 134–142, 2019.

[2] T. S. Rappaport *et al.*, "Wireless communications and applications above 100 GHz: Opportunities and challenges for 6G and beyond," *IEEE Access*, vol. 7, pp. 78 729–78 757, 2019.

[3] H. Tataria *et al.*, "6G wireless systems: Vision, requirements, challenges, insights, and opportunities," *Proc. IEEE*, vol. 109, no. 7, pp. 1166–1199, 2021.

[4] A. R. Chiriyath *et al.*, "Radar-communications convergence: Coexistence, cooperation, and co-design," *IEEE Trans. Cogn. Commun. Netw.*, vol. 3, no. 1, pp. 1–12, 2017.

[5] F. Liu *et al.*, "Integrated sensing and communications: Towards dual-functional wireless networks for 6G and beyond," 2021. [Online]. Available: https://arxiv.org/abs/2108.07165

[6] C. De Lima *et al.*, "Convergent communication, sensing and localization in 6G systems: An overview of technologies, opportunities and challenges," *IEEE Access*, vol. 9, pp. 26 902–26 925, 2021.

[7] H. Wymeersch *et al.*, "Integration of communication and sensing in 6G: a joint industrial and academic perspective," 2021. [Online]. Available: https://arxiv.org/abs/2106.13023

[8] D. K. Pin Tan *et al.*, "Integrated sensing and communication in 6G: Motivations, use cases, requirements, challenges and future directions," in *Proc. 1st IEEE Int. Online Symp. Joint Commun. Sens. (JC&S)*, 2021, pp. 1–6.

[9] Q. Wu *et al.*, "Intelligent reflecting surface-aided wireless communications: A tutorial," *IEEE Trans. Commun.*, vol. 69, no. 5, pp. 3313–3351, 2021.

[10] A. Elzanaty *et al.*, "Towards 6G holographic localization: Enabling technologies and perspectives," 2021. [Online]. Available: https://arxiv.org/abs/2103.12415

[11] H. Wymeersch *et al.*, "Radio localization and mapping with reconfigurable intelligent surfaces: Challenges, opportunities, and research directions," *IEEE Veh. Technol. Mag.*, vol. 15, no. 4, pp. 52–61, 2020.

[12] E. Basar *et al.*, "Wireless communications through reconfigurable intelligent surfaces," *IEEE Access*, vol. 7, pp. 116 753–116 773, 2019.

[13] C. Pan *et al.*, "Reconfigurable intelligent surfaces for 6G systems: Principles, applications, and research directions," *IEEE Commun. Mag.*, vol. 59, no. 6, pp. 14–20, 2021.

[14] X. Yuan *et al.*, "Reconfigurable-intelligent-surface empowered wireless communications: Challenges and opportunities," *IEEE Wireless Commun.*, vol. 28, no. 2, pp. 136–143, 2021.

[15] C. Huang *et al.*, "Reconfigurable intelligent surfaces for energy efficiency in wireless communication," *IEEE Trans. Wireless Commun.*, vol. 18, no. 8, pp. 4157–4170, 2019.

[16] D. Dardari *et al.*, "LOS/NLOS near-field localization with a large reconfigurable intelligent surface," *IEEE Transactions on Wireless Communications*, vol. 21, no. 6, pp. 4282–4294, 2022.

[17] Z. Yang *et al.*, "Energy-efficient wireless communications with distributed reconfigurable intelligent surfaces," *IEEE Trans. Wireless Commun.*, vol. 21, no. 1, pp. 665–679, 2022.

[18] B. Di *et al.*, "Hybrid beamforming for reconfigurable intelligent surface based multi-user communications: Achievable rates with limited discrete phase shifts," *IEEE J. Sel. Areas Commun.*, vol. 38, no. 8, pp. 1809–1822, 2020.

[19] C. Huang *et al.*, "Reconfigurable intelligent surface assisted multiuser MISO systems exploiting deep reinforcement learning," *IEEE J. Sel. Areas Commun.*, vol. 38, no. 8, pp. 1839–1850, 2020.

[20] H. Guo *et al.*, "Weighted sum-rate maximization for reconfigurable intelligent surface aided wireless networks," *IEEE Trans. Wireless Commun.*, vol. 19, no. 5, pp. 3064–3076, 2020.

[21] Z. Zhou *et al.*, "Joint transmit precoding and reconfigurable intelligent surface phase adjustment: A decomposition-aided channel estimation approach," *IEEE Trans. Commun.*, vol. 69, no. 2, pp. 1228–1243, 2021.

[22] Q. Wu *et al.*, "Intelligent reflecting surface enhanced wireless network via joint active and passive beamforming," *IEEE Trans. Wireless Commun.*, vol. 18, no. 11, pp. 5394–5409, 2019.

[23] M.-M. Zhao *et al.*, "Outage-constrained robust beamforming for intelligent reflecting surface aided wireless communication," *IEEE Trans. Signal Process.*, vol. 69, pp. 1301–1316, 2021.

[24] S. Hu *et al.*, "Beyond massive MIMO: The potential of positioning with large intelligent surfaces," *IEEE Trans. Signal Process.*, vol. 66, no. 7, pp. 1761–1774, 2018.

[25] K. Keykhosravi *et al.*, "SISO RIS-enabled joint 3D downlink localization and synchronization," in *IEEE Int. Conf. Commun.*, 2021, pp. 1–6.

[26] A. Elzanaty *et al.*, "Reconfigurable intelligent surfaces for localization: Position and orientation error bounds," *IEEE Trans. Signal Process.*, vol. 69, pp. 5386–5402, 2021.

[27] Z. Abu-Shaban *et al.*, "Near-field localization with a reconfigurable intelligent surface acting as lens," in *IEEE Int. Conf. Commun.*, 2021, pp. 1–6.

[28] O. Rinchi *et al.*, "Compressive near-field localization for multipath RIS-aided environments," *IEEE Communications Letters*, pp. 1–1, 2022.

[29] F. Guidi *et al.*, "Radio positioning with EM processing of the spherical wavefront," *IEEE Trans. Wireless Commun.*, vol. 20, no. 6, pp. 3571–3586, 2021.

[30] M. Rahal *et al.*, "RIS-enabled localization continuity under near-field conditions," in *Proc. IEEE 22nd Int. Workshop Signal Process. Adv. Wireless Commun. (SPAWC)*, 2021, pp. 436–440.

[31] A. Guerra *et al.*, "Near-field tracking with large antenna arrays: Fundamental limits and practical algorithms," *IEEE Transactions on Signal Processing*, vol. 69, pp. 5723–5738, 2021.

[32] M. Rahal *et al.*, "Constrained RIS phase profile optimization and time sharing for near-field localization," 2022. [Online]. Available: https://arxiv.org/abs/2203.07269

[33] Z. Wang *et al.*, "Location awareness in beyond 5G networks via reconfigurable intelligent surfaces," *IEEE J. Sel. Areas Commun.*, pp. 1–1, 2022.

[34] K. Keykhosravi *et al.*, "Multi-RIS discrete-phase encoding for interpath-interference-free channel estimation," 2021. [Online]. Available: https://arxiv.org/abs/2106.07065

[35] S. Abeywickrama *et al.*, "Intelligent reflecting surface: Practical phase shift model and beamforming optimization," *IEEE Trans. Commun.*, vol. 68, no. 9, pp. 5849–5863, 2020.

[36] P. Xu *et al.*, "Reconfigurable intelligent surfaces-assisted communications with discrete phase shifts: How many quantization levels are required to achieve full diversity?" *IEEE Wireless Commun. Lett.*, vol. 10, no. 2, pp. 358–362, 2021.

[37] G. Gradoni *et al.*, "End-to-end mutual coupling aware communication model for reconfigurable intelligent surfaces: An electromagnetic-compliant approach based on mutual impedances," *IEEE Wireless Commun. Lett.*, vol. 10, no. 5, pp. 938–942, 2021.

[38] W. Wang *et al.*, "Joint beam training and positioning for intelligent reflecting surfaces assisted millimeter wave communications," *IEEE Trans. Wireless Commun.*, vol. 20, no. 10, pp. 6282–6297, 2021.

[39] J. He *et al.*, "Channel estimation for RIS-aided mmWave MIMO systems via atomic norm minimization," *IEEE Transactions on Wireless Communications*, vol. 20, no. 9, pp. 5786–5797, 2021.

[40] Y. Zhang *et al.*, "Performance analysis of RIS-aided systems with practical phase shift and amplitude response," *IEEE Trans. Veh. Technol.*, vol. 70, no. 5, pp. 4501–4511, 2021.

[41] S. Fortunati *et al.*, "Performance bounds for parameter estimation under misspecified models: Fundamental findings and applications," *IEEE Signal Process. Mag.*, vol. 34, no. 6, pp. 142–157, 2017.

[42] C. D. Richmond *et al.*, "Parameter bounds on estimation accuracy under model misspecification," *IEEE Trans. Signal Process.*, vol. 63, no. 9, pp. 2263–2278, 2015.

[43] C. Ozturk *et al.*, "On the impact of hardware impairments on RIS-aided localization," in *IEEE Int. Conf. Commun.*, 2022. [Online]. Available: www.ee.bilkent.edu.tr/%7Egezici/ICC.pdf

[44] S. Fortunati *et al.*, "Chapter 4: Parameter bounds under misspecified models for adaptive radar detection," in *Academic Press Library in Signal Processing, Volume 7*, R. Chellappa *et al.*, Eds. Academic Press, 2018, pp. 197–252.

[45] H. Zhang *et al.*, "Towards ubiquitous positioning by leveraging reconfigurable intelligent surface," *IEEE Commun. Lett.*, vol. 25, no. 1, pp. 284–288, 2021.

[46] T. A. Milligan, *Modern antenna design*. John Wiley & Sons, 2005.

[47] B. Friedlander, "Localization of signals in the near-field of an antenna array," *IEEE Transactions on Signal Processing*, vol. 67, no. 15, pp. 3885–3893, 2019.

[48] J.-W. Tao *et al.*, "Joint DOA, range, and polarization estimation in the Fresnel region," *IEEE Transactions on Aerospace and Electronic Systems*, vol. 47, no. 4, pp. 2657–2672, 2011.

[49] V. R. Gowda *et al.*, "Wireless power transfer in the radiative near field," *IEEE Antennas and Wireless Propagation Letters*, vol. 15, pp. 1865–1868, 2016.

[50] B. O. Zhu *et al.*, "Active impedance metasurface with full 360 reflection phase tuning," *Scientific reports*, vol. 3, no. 1, pp. 1–6, 2013.

[51] L. Dai *et al.*, "Reconfigurable intelligent surface-based wireless communications: Antenna design, prototyping, and experimental results," *IEEE Access*, vol. 8, pp. 45 913–45 923, 2020.

[52] S. Sun *et al.*, "Gradient-index meta-surfaces as a bridge linking propagating waves and surface waves," *Nature materials*, vol. 11, no. 5, pp. 426–431, 2012.

[53] C. L. Holloway *et al.*, "An overview of the theory and applications of metasurfaces: The two-dimensional equivalents of metamaterials," *IEEE Antennas and Propagation Magazine*, vol. 54, no. 2, pp. 10–35, 2012.

[54] K. Zhi *et al.*, "Uplink achievable rate of intelligent reflecting surface-aided millimeter-wave communications with low-resolution ADC and phase noise," *IEEE Wireless Communications Letters*, vol. 10, no. 3, pp. 654–658, 2021.

[55] J. V. Alegría *et al.*, "Cramér-Rao lower bounds for positioning with large intelligent surfaces using quantized amplitude and phase," in *2019 53rd Asilomar Conference on Signals, Systems, and Computers*, 2019, pp. 10–14.

[56] T. T. Le *et al.*, "Misspecified Cramer-Rao bounds for blind channel estimation under channel order misspecification," *IEEE Trans. Signal. Process.*, pp. 1–1, 2021.

[57] F. Roemer, "Misspecified Cramer-Rao bound for delay estimation with a mismatched waveform: A case study," in *IEEE Int. Conf. Acoustics, Speech Signal Process.*, 2020, pp. 5994–5998.

[58] Y. Wang *et al.*, "Super-resolution channel estimation for arbitrary arrays in hybrid millimeter-wave massive MIMO systems," *IEEE Journal of Selected Topics in Signal Processing*, vol. 13, no. 5, pp. 947–960, 2019.

[59] A. A. Cuyt *et al.*, *Handbook of Continued Fractions for Special Functions*, 1st ed. Springer Publishing Company, Incorporated, 2008.

[60] A. Swindlehurst *et al.*, "Maximum likelihood methods in radar array signal processing," *Proceedings of the IEEE*, vol. 86, no. 2, pp. 421–441, 1998.

[61] A. Aubry *et al.*, "A new sequential optimization procedure and its applications to resource allocation for wireless systems," *IEEE Transactions on Signal Processing*, vol. 66, no. 24, pp. 6518–6533, 2018.